Molybdenum Disulphide (MoS_2)-Poly(3-hexylthiophene) (P3HT) Hybrid Ink for Printed Thin-Film Transistor Applications

by

Naeun Kim

A thesis

presented to the University of Waterloo

in fulfillment of the

thesis requirements for the degree of

Master of Applied Science

in

Electrical & Computer Engineering

Waterloo, Ontario, Canada, 2020

Author's declaration

I hereby declare that I am the sole author of this thesis. This is a true copy of the thesis, including any required final revisions, as accepted by my examiners.

I understand that my thesis may be made electronically available to the public.

Abstract

Organic Thin-Film Transistors (OTFTs) based on Poly(3-hexylthiophene) (P3HT)-Molybdenum Disulphide (MoS_2) composite films as an active layer were prepared via inkjet printing. There have been many attempts to incorporate inorganic materials into organic semiconductors, however, the inkjet-printed MoS_2-P3HT hybrid ink for Thin-Film Transistor (TFT) applications is shown here for the first time. The P3HT-MoS_2 hybrid TFTs exhibited higher carrier mobility than the baseline TFT with pure P3HT. We assume this is attributed to the molecular ordering of P3HT improved with the existence of MoS_2 nanoparticles in the film and also the high hole carrier mobility of MoS_2 could act as a conducting bridge.

In this research, the first step was to improve overall TFT performance by optimizing the OTFT process conditions. Various factors were examined including surface treatment, solution preparation, and post-processing to change the crystallization of polymer film through different process conditions. It was shown that the Self-Assembled Monolayer (SAM) treatment could give preferred molecular orientation to the film; the selection of organic solvents is important because their boiling point affects film formation; the film thickness and post-processing conditions also affect the mobility as well as the off-current.

Meanwhile, the MoS_2-P3HT hybrid ink was formulated with simple steps. This ink was prepared for inkjet printing. The jetting and printing parameters are precisely controlled to enable the printing of a hybrid channel array on top of pre-patterned electrodes. Especially, the ink should be compatible with selected nozzles, otherwise, the nozzle can be blocked or the misprint may cause device failure. The TFTs with a MoS_2-P3HT hybrid channel were successfully fabricated via inkjet printing. With the incorporation of MoS_2 nanoparticles, the hybrid TFTs exhibit mobility as high as 2.35×10^{-2} $cm^2/V\text{-}s$ which is more than two times higher than the P3HT-only TFTs while maintaining the on/off ratios and threshold voltages.

Acknowledgements

It is a genuine pleasure to express gratitude and appreciation to my supervisor, Professor William Wong, for the continuous support and guidance throughout my research. Professor Wong always gave me an insight and motivations which fulfilled my interests in scientific research and desire to go forward. Thank you again for all the opportunities given to me, especially, introducing me to printed electronics.

I would like to thank my colleagues, Advanced Flexible Electronics Technology (AFET) group members, for their thoughtful advices and cares. Thanks to Mohammad Nouri for introducing and training me all the equipment, thanks to Hyunwoo Choi for sharing me valued experiences in research, thanks to Wontae Park for equipping me with knowledge in organic transistors, thanks to Mohsen Asad, Kendall Davis, Qing Li and Matan Winstok for advices both scientific and life. It was warm and enjoyable times working and spending time with all the members.

I would like to express my gratitude to Richard Barber and Dr. Czang-Ho Lee for the training and support provided inside and outside the Giga-to-Nanoelectronics (G2N) Lab which prepared me with the fundamentals during my research.

I would like to appreciate Professor Hany Aziz for the introduction to Organic Electronics, the great lecture and warm support had lasting effect. Thanks to Professor Yuning Li and group members who allowed me to use equipment and shared knowledge in organic thin-film transistors fabrication which was essential to proceed my research. Thanks to Professor Irene Goldthorpe, as a reader of this thesis, for valuable comments.

Finally, I must express my very profound gratitude to my parents for providing me with unfailing support and continuous encouragement throughout my study. This accomplishment would not have been possible without them.

Table of Contents

List of Figures

List of Tables

Part I Introduction

I.1 Introduction

Printed electronics are receiving great attention due to advantages in availabilities in flexible device integration, cost-effective processing, and large area production. Among printing methods, inkjet printing directly deposits material on the surface as a film or pattern without damage or contamination on the surface. Due to its additive process, ink-jet printing enables materials to be processed at room temperature for different applications such as memory, organic thin-film transistors (OTFT), organic light-emitting diodes (OLEDs), sensors, solar cells, and digital and analog circuits [1]–[8]. These applications are realized with solution-based inks, especially, semiconducting polymers. However, organic semiconductors typically suffer from low carrier transport due to their amorphous nature. Although immense progress has been made to improve carrier mobility, high demands for solution-processed materials with outstanding performance still exist. In contrast to organic materials, inorganic materials exhibit high mobility with highly crystallized structures. Especially, two-dimensional (2D) materials, such as graphene and MoS_2, have gathered interests due to its high field-effect mobility, with good flexibility, transparency, and high stability oriented from their single atom thickness.

Recently, there have been attempts to solution process 2D materials in a nanoflake form and incorporate into organic semiconductors [9], [10], [11], [12]. The TFTs fabricated with organic-inorganic composites generally show improvement in electrical characteristics. However, this novel approach to device fabrication is not well established, with TFTs displaying high threshold voltage and low on/off current ratio [13]. Moreover, there are very few reports to print composite solutions. These issues will be more discussed in I.6.2. Here, the development for a formulation process to create an organic-inorganic hybrid ink is presented, with the formulated ink used in fabricating hybrid TFTs via inkjet printing.

I.2 Organic thin-film transistors (OTFTs)

A thin-film transistor (TFT) is a branch of a MOSFET (metal-oxide-semiconductor field-effect transistor) device. The active semiconductor layer of the TFT is a thin-film that differs from conventional MOSFET, where a single-crystal silicon substrate is used as the active semiconductor layer. A variation of the TFT is the organic thin-film transistors (OTFTs) that are transistors based on organic thin films that may be processed in solution form, allowing the semiconductor to be deposited as an electronic ink. OTFTs have gathered interests since 1980s for its potential in low-cost, large-area and flexible electronics [14], [15], [16]. The OTFT is also an alternative device structure for investigating charge transport in organic materials.

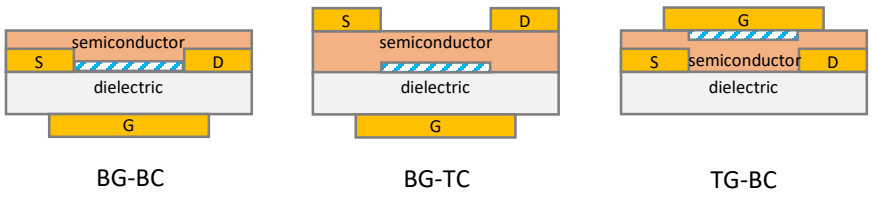

Figure I-1 OTFT device structures: bottom gate, bottom contacts (BG-BC); bottom gate, top contacts (BG-TC); top gate, bottom contacts (TG-BC). S: source; D: drain; G: gate. The active area of the transistor at the semiconductor dielectric interface is indicated (*i.e.* blue diagonal region).

The structure of the OTFT device is mainly composed of electrodes (gate, source, and drain), semiconductor, and dielectric as depicted in **Figure I-1**. The OTFT components can be structured differently by fabrication methods to realize desired properties. The devices mainly operate on accumulation mode. When the gate electrode is biased by a gate voltage, V_G, an electric field is created through a thin-film dielectric layer to attract charge existing in the semiconductor. The attracted charges are accumulated at the semiconductor dielectric interface that increased the conductivity of the semiconductor, forming a conducting channel region at the interface. In the case of a p-channel transistor, negative voltage is applied to the gate and holes accumulate at the interface making a conducting path for hole carriers to flow.

The source and drain electrodes inject and retrieve hole carriers to and from the semiconductor. When applying a voltage between the source and the drain, the voltage difference creates an electric field acting parallel to the channel where carrier transport creates current flow between the source and drain contacts. However, in actual devices, mobile carriers are not immediately introduced into semiconductor film at $V_G = 0$ V. The gate-to-drain voltage V_{GD} should go beyond a threshold voltage, V_T, in order to start flowing current. The threshold voltage is affected by charge captured in trap states within the semiconductor and the dielectric-semiconductor interface [17], [18].

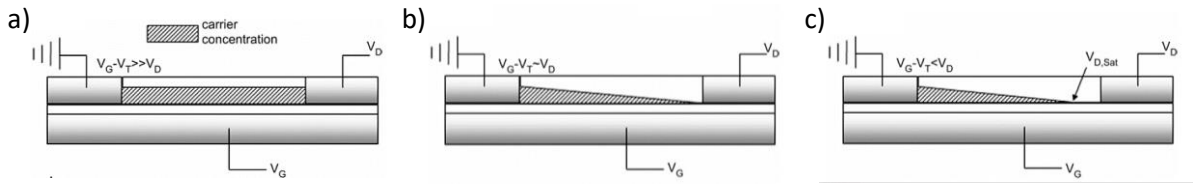

Figure I-2 a) Carrier concentration of TFT in the linear regime. b) Pinch-off occurs when V_D reaches V_G - V_T. c) Carrier concentration of TFT in the saturation regime [19]. *Reprinted (adapted) with permission from (Chem. Mater. 2004, 16, 23, 4436-4451). Copyright (2004) American Chemical Society.*

Figure I-2 shows carrier concentration in the channel as different drain voltage V_D and gate voltage V_G applied. When no voltage is applied to the drain, the density of accumulated carriers is uniform along the channel for a given V_G. Until V_D reaches the level of V_G, the accumulated charge is uniform across the channel length, where the TFT operates in the so-called linear regime (**Figure I-2.a**). The drain current I_D increases linearly with V_D in this regime. Once V_D exceeds V_G-V_T, the potential near the drain electrode falls to zero and the channel is pinched off (**Figure I-2.b**). A further increase in V_D moves the pinch point further from the drain electrode, but not significantly (**Figure I-2.c**). At this point, the drain current saturates which means I_D is independent of V_D [19], [20].

These relations can be explained in an equation, based on the gradual-channel approximation, which assumes that the voltages vary gradually along the channel region. The

drain current in the linear and saturation regimes are given without derivation in equations (1) and (2), respectively.

$$I_D = \frac{W}{L} C_{ox} \mu \left(V_G - V_T - \frac{V_D}{2} \right) V_D, \quad V_D < V_G - V_T \qquad (1)$$

$$I_{D_{sat}} = \frac{W}{2L} C_{ox} \mu_{sat} (V_G - V_T)^2, \qquad V_D > V_G - V_T \qquad (2)$$

W and L are the width and the length of the channel, C_{ox} and μ are the gate oxide capacitance and field-effect mobility, respectively.

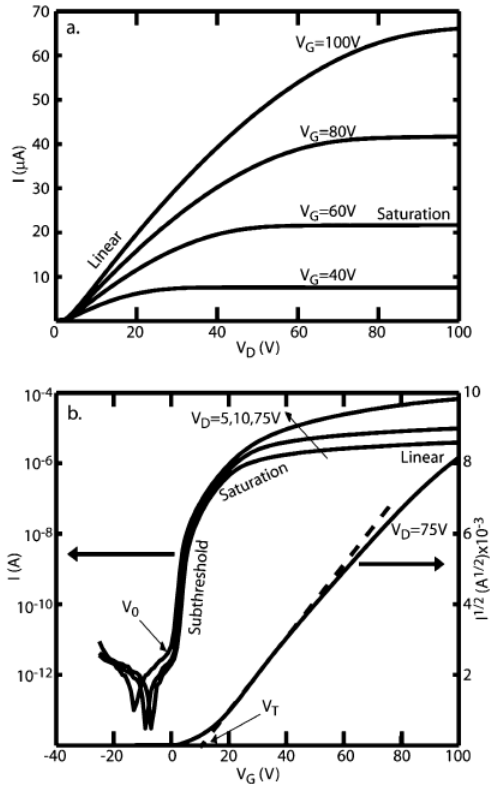

Figure I-3 a) Example I_D-V_D curves for various values of V_G. b) Example I_D-V_G curves plotted on logarithmic scale for various values of V_D (left axis), and square root I_D with varying V_G (right axis) [19]. *Reprinted (adapted) with permission from (Chem. Mater. 2004, 16, 23, 4436-4451). Copyright (2004) American Chemical Society.*

OTFTs are typically characterized in two ways. The transfer curve, I_D vs. V_G, is measured by sweeping V_D with a constant V_G (**Figure I-3.b**), and the output curve, I_D vs. V_D, is measured by sweeping V_G with a constant V_D (**Figure I-3.a**). However, if a contact resistance exists, the near-zero I_D-V_D graph may show non-linear characteristics or the square root I_D graph rolls down at high V_G [19], [20].

The key parameters evaluating the electrical characteristics of the OTFT are mobility, threshold voltage, subthreshold swing, and on/off ratio. These parameters determine the switching speed, the power consumption, and the switching capability of the devices. Here, we used the saturation current equation and the transfer curve in a square root and a logarithmic form to extract parameters: the mobility is obtained from the slope of the $\sqrt{I_{D_{sat}}}$–V_G curve, the threshold voltage is estimated from the extrapolation of the I_D–V_G curve when $I_D = 0$; the subthreshold swing is correlated to the steepest slope of logarithmic I_D–V_G plot; the on-off ratio refers to the ratio of the highest on current to the lowest off-current.

I.3 OTFT processing

Figure I-4 depicts a typical bottom-gate top-contact (BG-TC) OTFT architecture with a spin-coated semiconducting polymer film on top of source-drain electrodes. The spin-coating method can be replaced by printing methods. This structure is beneficial for OTFTs, because the organic semiconductor is deposited last, minimizing the effects of other processes for degrading the quality of the organic film. The device fabrication procedure used in the experiments is described as follows.

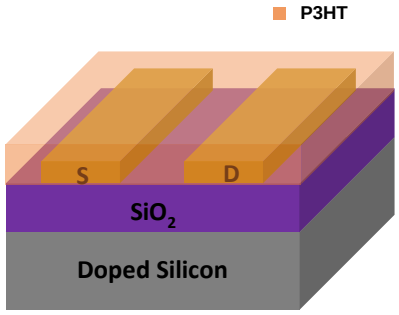

Figure I-4 Schematic device structure of a spin-coated P3HT TFT having a bottom-gate, bottom-contacts structure.

1. Electrodes patterning

Highly doped p-type silicon substrates were used as the common bottom gate structure with thermally grown 100 nm thickness silicon dioxide as a dielectric layer. The source and drain electrodes are patterned by conventional photolithography following a fabrication process shown in **Figure I-5**. The electrodes are defined using photolithography to create an electrode array with devices having various channel lengths from 10 to 150 μm with a constant channel width of 1000 μm (**Figure I-6**). Devices having a 30 μm channel length patterns were used for characterizing the fabricated devices. 2 nm Cr and 40 nm Au were thermally deposited as an adhesion layer for the Au and as the contact layer, respectively. The patterned substrates are diced into 17 mm × 17 mm small individual dies containing 36 transistors.

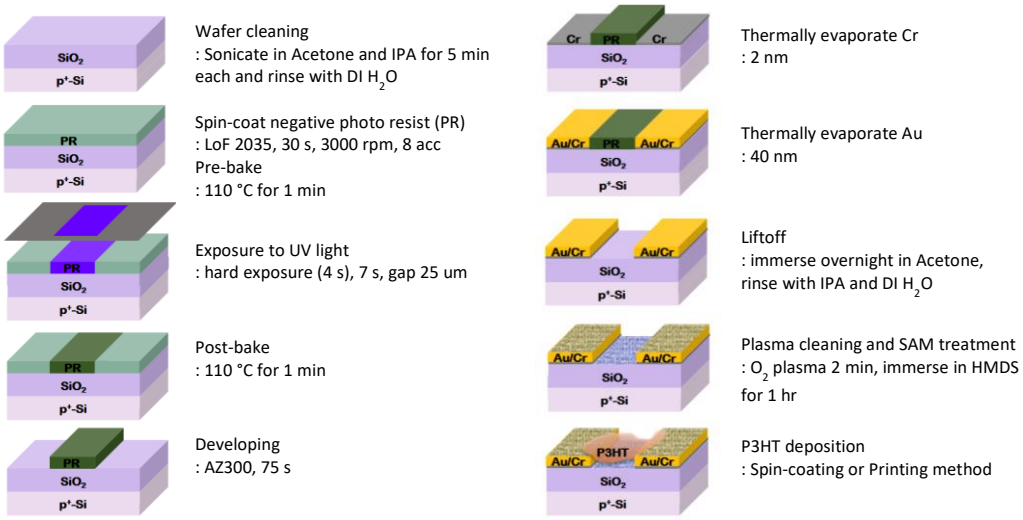

Figure I-5 Conventional photolithography based bottom-gate bottom-contact (BG-TC) OTFT fabrication process. A highly doped Si with oxide layer is solution-cleaned; a negative photoresists is spin-coated on the substrate; the resist is pre-baked, exposed to UV with a patterned photo mask, then post-baked; the substrate is soaked in a developer to remove the resist that were not exposed; Cr and Au are thermally evaporated onto the substrate; the substrate is soaked in acetone to liftoff metals on non-pattern parts; clean the substrate with plasma, then SAM formulated; an organic semiconductor, P3HT, is deposited on top of Au electrodes.

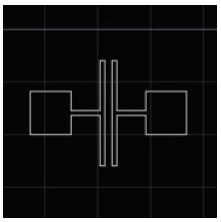

Figure I-6 Photo mask design of source-drain electrodes with the dimension of L = 50 um and W = 1000 um.

2. Self-assembled monolayer (SAM) treatment

Electrodes-patterned SiO_2 substrates were cleaned by sonication in acetone and IPA for 5 min each, rinsed with distilled (DI) water, then blow-dried with nitrogen. The cleaned substrate was then treated with oxygen plasma for 2 min using a Plasma cleaner, PDC-32G (Harrick Plasma, USA). The oxygen plasma effectively oxidizes remaining organics or gas

and water molecules attached on the surface into volatile molecules and the vacuum evacuates all the products [21]. Then, the substrate is ready for surface functionalization using molecular monolayer to change the surface properties of the substrate.

Self-assembled monolayers (SAM) are molecular assemblies formed on surfaces. A new functional group has an affinity for the substrate attaches to the substrate surface to tailor the interfacial properties of the surface **Figure I-7.** Different head groups bind to specific metals, metal oxides, and semiconductors. However, the head groups can react with contaminants and impurities before displacing the surface atom which means the substrate cleanness and the purity of solutions are important to form the SAM efficiently [22]. Thus, the plasma cleaning is preferred when preparing the substrate.

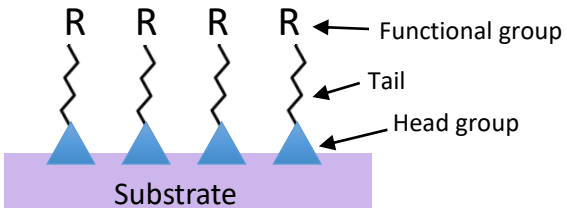

Figure I-7 An illustration of a typical self-assembled monolayer (SAM). SAM materials composed of a functional group and a tail attached to the head group of a substrate surface. The functional group determines the new chemical properties of SAM treated substrate.

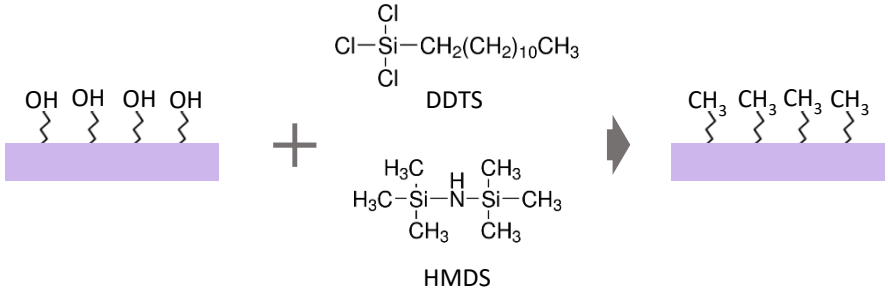

Figure I-8 An illustration of hydroxyl group (-OH) of a SiO_2 surface displaced into methyl group (-CH_3) when DDTS or HMDS is applied.

SAM treatment is known to improve the electrical performance of OTFTs significantly by enhancing the crystallinity of organic semiconducting film [23], [24]. OTFT performance largely affected by the semiconductor-dielectric interface conditions and SAM effectively controls the chemistry of the interface [25]. SAM materials with alkyl chains help alignment of polymer molecules into an edge-on orientation which correlates to the fast charge transport direction in the semiconductor structure, as well as forming larger and uniform crystalline domains [24], [26]. **Figure I-8** shows a displacement of hydroxyl group (-OH) into methyl group ($-CH_3$) with the exposure to the oxide layer modification agents, dodecyltrichlorosilane (DDTS) and hexamethyldisilazane (HMDS). After the displacement, the surface reveals hydrophobicity which is brought by methyl groups [27].

These materials also can be used to modify overall surface energy and wettability. When depositing polymer film on gold patterned SiO_2 substrate, the different surface energies between gold and SiO_2 can hinder the overall crystallinity of the film by affecting the wetting and subsequent solvent evaporation in polymeric solution as the film forms. Although gold is known to be stable in the air, some studies showed gold oxidized into Au_2O_3 in ambient conditions [28], [29]. This oxide layer provides adhesion groups for SAM materials with alkyl chains. Eventually, the overall surface will have a similar level of surface energy and wettability if both the metal and dielectric surfaces of the TFT structure are functionalized before the semiconductor ink is applied.

In this work, the SAM modifies the SiO_2 surface, and hexamethyldisilazane (HMDS) (Sigma-Aldrich) was chosen as the SAM material. The substrate is immersed in HMDS solution for 12 hours preferably, but can be reduced to 1 hour once a chemically uniform surface is prepared, then rinsed with toluene and blow-dried with nitrogen. Now the modified surface is hydrophobic, typically with the water contact angle larger than 90°, you can observe that toluene hardly wets the surface. The effect of SAM and the evaluation of SAM treatment time will be more discussed in II.1.1.

3. P3HT solution preparation

The organic polymer, poly(3-hexylthiophene) (P3HT) (95.7 % regioregularity, Ossila), was dissolved in 1,2-dichlorobenzene (Sigma-Aldrich) while the solution was heated to 85 °C for 1 hr on a hotplate. 1,2-dichlorobenzene was filtered ahead with a 0.45 μm PTFE filter to remove possible contaminants or dust. The concentration of P3HT solution was 10 mg/ml. The solution was prepared in an N_2 environment, protected from exposure to UV light and processed shortly after preparation.

1,2-dichlorobenzene was chosen as an organic solvent for its high boiling point 180 ℃, compared to other typical organic solvents such as chloroform with 60 ℃ and chlorobenzene of 120 ℃. The boiling point is closely related to the time available for polymer chains to align when they are still in solution. In other words, slow evaporation of solvent with a high boiling point results in a film having a higher crystalline order with stronger inter-chain interactions [30].

4. Film deposition by spin-coating and printing

To create reference devices for comparison to inkjet printed TFTs, the P3HT film was spin-coated on the HMDS-treated surface at 3000 rpm for 80 s and with an acceleration rate of 800 rpm/s in a nitrogen ambient. This spin-coating condition gives a ~50 nm thickness film after spinning. Since 1,2-dichlorobenzene has a high boiling point, the spin-coating time should be long enough to completely dry the film during spinning. Some studies show the effect of film thickness on the charge carrier mobility of P3HT TFTs [31], [32]. Referring to these studies, field-effect mobility increases as P3HT layer gets thicker for thicknesses up to 50nm. Further increase in thickness may improve the mobility in a small scale, but deteriorates device performance by increasing the off-current. This is due to the fact that the voltage applied to the gate only can control the depletion of charge near the dielectric-semiconductor interface and current flows in thicker films due to bulk conductivity [31].

The OTFT fabrication layers can be produced by printing methods to deposit the dielectric, electrodes, and semiconductor. Since our TFTs are fabricated on the Si/SiO_2 substrate that corresponds to the gate/dielectric layers, the electrode or the semiconductor layer or either can be deposited using printing methods. **Figure I-9** shows the fabrication process of OTFTs by printing electrodes and the active layer sequentially. The solution preparation and post-annealing procedure are the same with spin-coated P3HT TFTs. However, silver electrodes printed with silvernanoparticle (AgNP) ink need to be sintered at 200 °C for 30 min under a nitrogen ambient. This temperature and time give enough heating energy for nanoparticles to sinter and become a continuous metallic thin film.

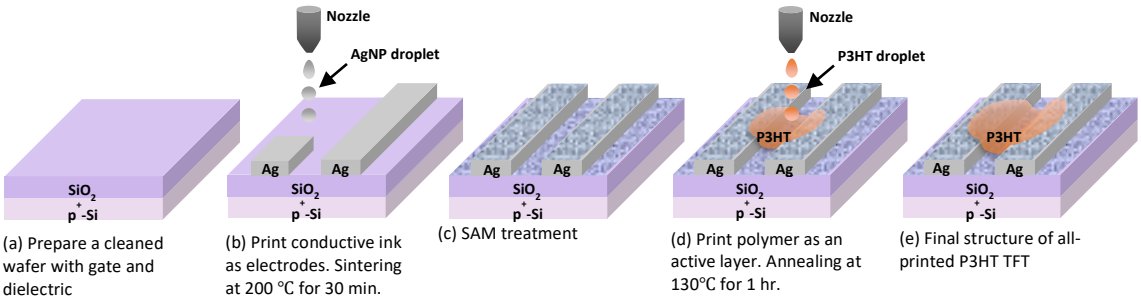

Figure I-9 P3HT TFTs fabrication process with electrodes and semiconductor layer deposited via inkjet printing. A highly doped Si with oxide layer is solution-cleaned; electorde patterns are printed with silvernanoparticle (AgNP) ink and sintered; the patterned substrate is treated with SAM material; an organic semiconductor, P3HT, is printed on top of Ag electrodes and post-processed.

5. Post-processing

The devices were then oven-annealed in vacuum for 1 hr at 120°C, which is slowly ramped up from the room temperature.

OTFTs annealed in an ambient atmosphere is known to show lower performance than those processed in an inert atmosphere, because of sensitivity to doping by atmospheric oxygen [26], [33], [34]. Especially, the P3HT film is highly affected by the processing environment. The π-π stacking distance of P3HT is 3.7 Å which is larger enough for extrinsic

molecules such as oxygen and water to diffuse into P3HT film and degrade the electrical performance of fabricated TFTs [35], [31].

6. Measurement

The fabricated devices **Figure I-10** are characterized using pulsed voltage inputs to measure the current-voltage (I-V) characteristics. The measurements were performed using a Keithley 2400 under vacuum and dark conditions. However, this measurement setup only measures down to nano-ampere currents, limiting the measurement of the off current down by at least three orders of magnitude. To measure smaller currents, a Keithely 6430 picoammeter was used under dc voltage condition; the P3HT TFTs off current generally goes down to 10^{-12} A. However, the Keithely 6430 is only compatible with dc-biasing, which may result in reducing the electrical stability of the devices. Pulse-biasing prevents organic films from degrading by shorter gate-voltage stressing times, and the pulsed gate voltage help maintain a constant threshold voltage. For this reason, the Keithley 2400 was used for the subsequent device I-V characterization.

The voltage settings are indicated in 'device fabrication process' section of each chapter.

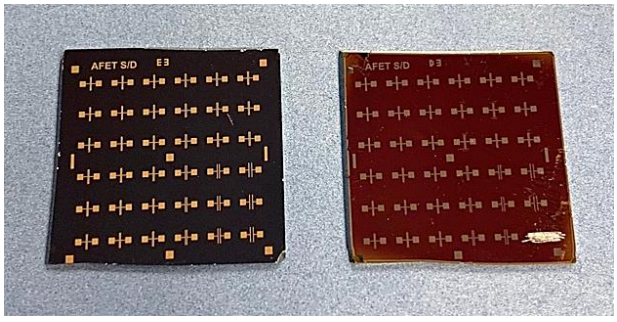

Figure I-10 Arrays of Au electrodes (left) and spin-coated P3HT TFTs (right).

I.4 Printing technology

I.4.1 Printing technology

Printed electronics are receiving great attention due to their potential to simultaneously deposit and pattern devices on various large-area substrates at low fabrication cost [36], [37], [38], [39]. Especially, transparent electronic devices formed on flexible substrates are expected to meet emerging technological demands where silicon-based electronics cannot provide a solution [40]. For these reasons, the initial work with printing technology has centered on displays and photovoltaics, which are fundamentally area-intensive applications and have a potential to be fabricated on flexible substrates. Research development areas presently include medical, wireless, sensing, flexible, and ultrathin applications. From a device point of view, these applications are mostly based on thin-film transistors as basis components; hence, the research in developing printed TFTs is worth investigating. Especially, organic materials have many advantages in printed TFT applications because they can be processed as a solution at low temperature.

Printing systems can be divided into two categories, contact printing and non-contact printing, as shown in **Figure I-11**. Contact printing, such as gravure printing, flexographic printing, and screen printing, is to print a pattern on the substrate in contact with the ink bath or dispenser. Gravure printing is a commonly used printing technique for printed electronics, for its high-resolution, high-throughput properties [41], [42]. However, due to its contact nature, the substrate or pre-deposited layer can be damaged or contaminated during the processing. Jet printing is beneficial for device fabrication in this manner. Inkjet printing and spray printing (aerosol jet printing), as a non-contact printing approach, inks are directly ejected from the nozzle to the substrate in a form of droplets or sprays. Above all, inkjet printing has been the most popularly used technology for thin-film electronics for its simplicity, low-cost operation, and free of damage or contamination to the surface [39], [13], [43], [44]. Moreover, complex multi-layer structures can be realized without the use of a

physical mask and because the designing is digitalized, customized production gives freedom for rapid prototyping of thin-film devices [45].

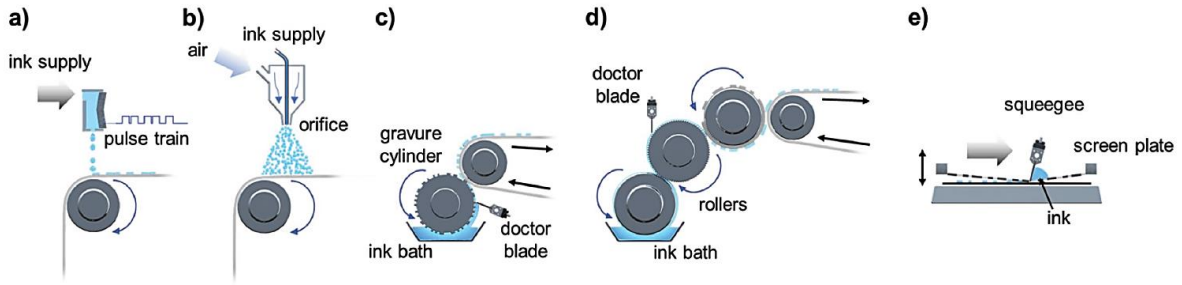

Figure I-11 Schematics of various printing techniques: a) inkjet printing, b) spray printing, c) gravure printing, d) flexographic printing, and e) screen printing [13]. *Copyright (2019) Seungjun Chung, Kyungjune Cho, and Takhee Lee.*

I.4.2 Inkjet printing

1. Inkjet printer

The following description of inkjet printer is written based on CeraPrinter F-serie (Ceradrop, France) shown in **Figure I-12**. The inkjet printer is composed of two parts: the operative part and the command part. The printer head, display module, and chuck are installed in the operative part and the command part consists of axes controller, printer motor, and pneumatic system. On the printer head carrier, three different inkjet dispensers are installed: Dimatix Materials Cartridge (Fuijfilm, USA), MicroFab single jet dispensing device (MicroFab, USA), and Q-Class (Fujifilm, USA) (**Figure I-13**). The aerosol system is also embedded but will not be discussed here. The aerosol jet has an advantage on jetting materials with high viscosity up to 1000 cP. However, the operation of the inkjet is much simple than the aerosol jet and the inks we use are compatible with inkjet printing, hence, we only used inkjet print heads for the TFT fabrication. The inkjet system is operated with different nozzle types including single and multi nozzles. Multi nozzles have up to a thousand nozzles. Cartridge and Q-Class are multi nozzles dispensers with 16 and 256 nozzles, respectively, and MicroFab is a single nozzle dispenser. The multi nozzle reduces time for printing a pattern

which enables large-area printing within a comparably short time. However, the single nozzle gives more freedom to a drop controlling and a vector printing. There is also a variety of nozzle diameter from 10 μm to 80 μm, and the droplet volume goes down to a few pl and up to ~200 pl in accordance with the nozzle size and the pulse setting.

Figure I-12 CeraPrinter F-serie printer system for process development in printed electronics.

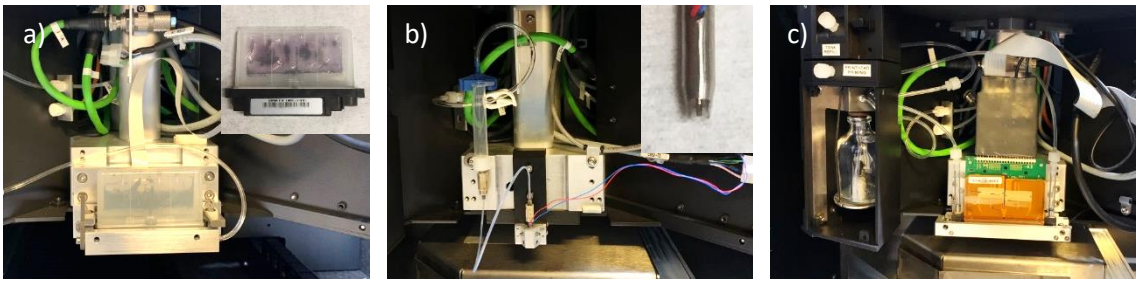

Figure I-13 Printer heads imbedded in CeraPrinter F-serie: a) Dimatix Materials Cartridge, b) MicroFab single jet dispensing device, and c) Q-Class.

2. Drop generation

The jetting can be controlled piezo-electrically, thermally, and electrostatically. However, the piezoelectric method is commonly used over thermal and electrostatic methods. This is mainly due to material degradation issue, limited solvents selection, and high running cost in thermal and electrostatic methods [46]. **Figure I-14** shows droplet ejection in piezoelectric

nozzles which operates based on a voltage pulse applied. **Figure I-15** shows an example of how the voltage is applied through a bipolar pulse waveform, where t_{rise}, t_{dwell}, t_{fall}, t_{echo}, and $t_{finalrise}$ are the periods consisting the waveform, and V_1, V_2, and V_{DC} are high, low, and center voltages, respectively. A positive change in voltage at t_{rise} and $t_{finalrise}$, the piezo-electric material (PZT) contracts which results in a negative liquid pressure (**Figure I-16**). Whereas, for a negative change of voltage at t_{fall}, the PZT expands and a positive liquid pressure is induced. Drops are formed when the pressure pulse is propagating in the fluid and the drop jets once the positive pressure exceeds a threshold level. The pressure amplitude is proportional to the ratio of voltage to time, which means the jetting correlates with both voltage and time setting [47]. The jetting is also controlled by a back pressure independent of the applied voltage to the PZT. The back pressure controls the ink meniscus at the nozzle orifice and helps keep the ink stable in the nozzle when no voltage pulse is applied [13], [48].

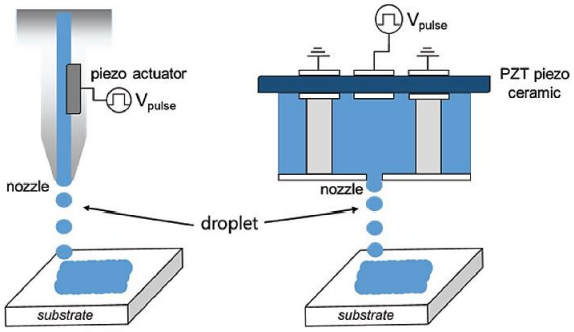

Figure I-14 Schematic of droplet ejection in piezoelectric nozzles: a single nozzle (left), and a cartridge-type nozzle (right) [13]. *Copyright (2019) Seungjun Chung, Kyungjune Cho, and Takhee Lee.*

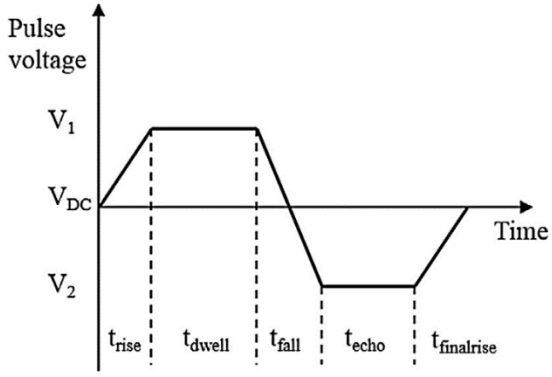

Figure I-15 Schematic of a bipolar pulse waveform [47]. *Reprinted (adapted) with permission from (Microelectronics Reliability 55 (2015) 630–636). Copyright (2014) Elsevier Ltd.*

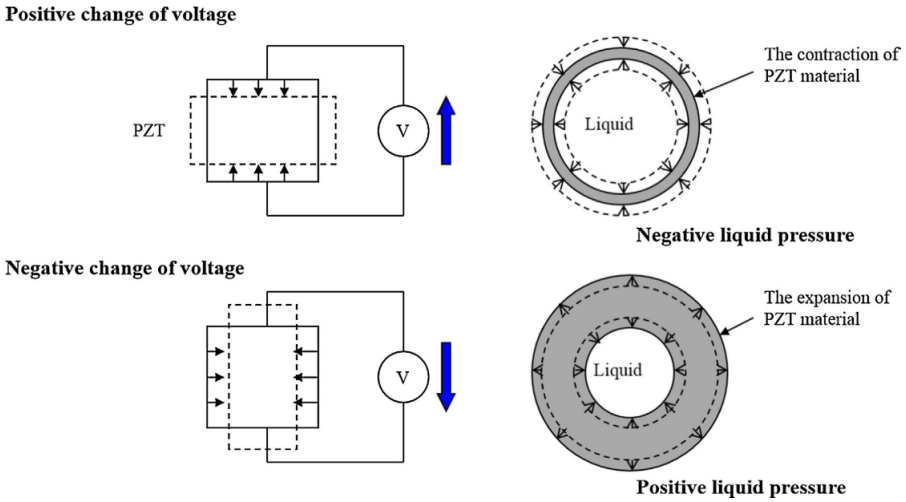

Figure I-16 Schematic illustration of operation principle of piezoelectric ink-jet printing with cross section in radial direction [47]. *Reprinted (adapted) with permission from (Microelectronics Reliability 55 (2015) 630–636). Copyright (2014) Elsevier Ltd.*

The generation of droplets can be characterized by the Reynolds number (Re), the Weber number (We), and the Ohnesorge number (Oh) [13], [48]:

$$Re = \frac{v\rho d}{\eta} \quad (1)$$

$$We = \frac{v^2 \rho d}{\gamma} \quad (2)$$

$$Oh = \frac{\sqrt{We}}{Re} = \frac{\eta}{\sqrt{\gamma \rho d}} \quad (3)$$

where v is the velocity of the ink, ϱ is the ink density, d is the nozzle diameter, η is the viscosity of the ink, and γ is the surface tension of the fluid. The Reynolds number is a relation between the inertial and viscous forces, and the Weber number is a relation between the inertial and surface tension forces. Both viscosity and surface tension can act as a barrier for ejection, and a sufficient energy is required to overcome these surface forces. The Ohnesorge number is derived from the Reynolds and Weber numbers, describing the printability, which is a relationship between the ink and the equipment. The inverse Ohnesorge number (Z = 1/Oh) is widely used to determine the range where stable drop forms, where $10 > Z > 1$ [39]. At low

Z, drops are too viscous for stable droplet ejection, whereas at high Z, satellites are observed in the droplet ejection due to low viscous forces in the inks (**Figure I-17**). However, exceeding the stable drop formation range, a stable droplet still can be generated with a precise pulse and backpressure settings. Although the inverse Ohnesorge number Z of water and ethanol is know to be a few hundred and a hundred, respectively, the stable jetting dynamics of water-ethanol mixture are shown in **Figure I-18** as a function of time. In these cases, the parameters may be experimentally chosen rather than modeled using dimensionless fluidic parameters.

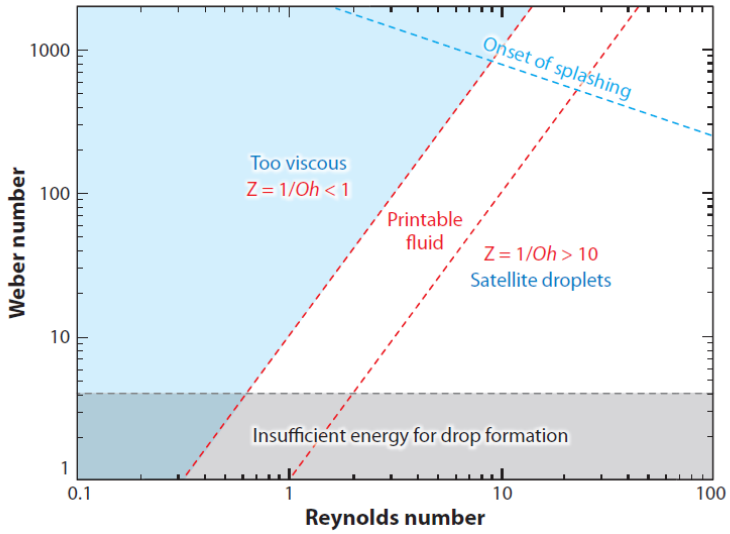

Figure I-17 A coordinate system defined by the Reynolds and Weber numbers describing the printability of fluids with the range of Z = 1/Oh [48]. *Copyright (2010) Annual Reviews.*

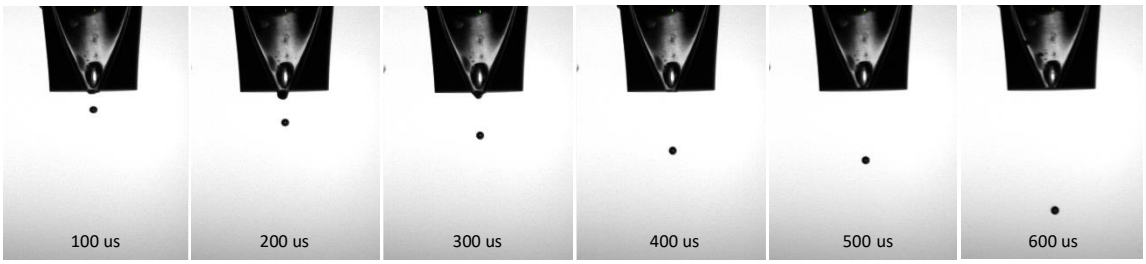

Figure I-18 Droplet generation of ethanol and water mixture as a function of time. The pulse waveform was t_{rise} = 2 μs, t_{dwell} = 4 μs, t_{fall} = 3 μs, t_{echo} = 8 μs, $t_{finalrise}$ = 2 μs, V_1 = 40 V, V_2 = -40 V, and V_{DC} = 5 V, and the back pressure was 12 kPa.

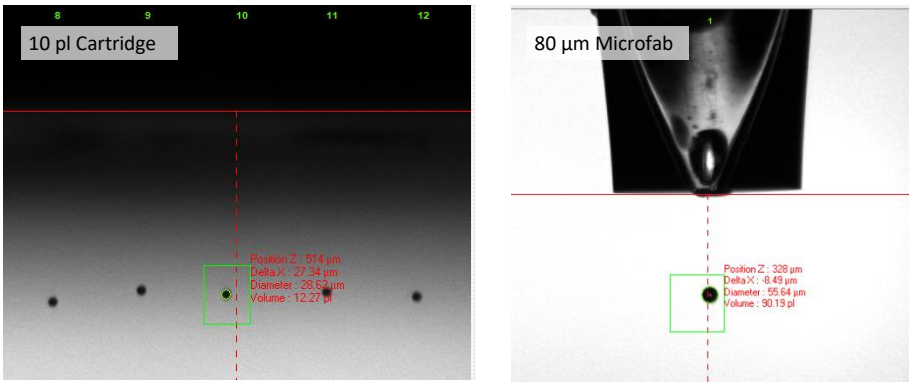

Figure I-19 Droplet analysis including diameter and volume on droplet generated from 10 pl Cartridge (left) and 80 µm Microfab (right). The drop diameter of 28.62 µm and the drop volume of 12.27 pl for 10 pl Cartridge, and the drop diameter of 55.64 µm and the drop volume of 90.19 pl for 80 µm Microfab.

Other than these parameters, the drop diameter follows the nozzle diameter in general, where the nozzle diameter and the drop volume are correlated as shown in **Figure I-19**. Experimentally, the drop volume of a 10 pl Cartridge (with a nozzle diameter ~10 µm) was 12.27 pl; whereas, the drop volume of 80 µm Microfab was 90 pl, which is not proportionally related but apparently limited by nozzle diameter.

In a material view, metal printing is relatively simple compared to polymer printing. Metal inks are compatible with both single and multi nozzles, especially with the multi ejector cartridge nozzle. Metal inks can be stored in the cartridge bag without any degradation or oxidation for more than a few months, thanks to their ligands protecting the ink and limited entry of air into the cartridge bag. In the case of polymers, extended storage time causes degradation of material quality, even when there is limited contact with the air as discussed in I.3. Hence, polymers are printed with a single ejector Microfab nozzle because the nozzle can be reused and the post-printing clean-up is simple.

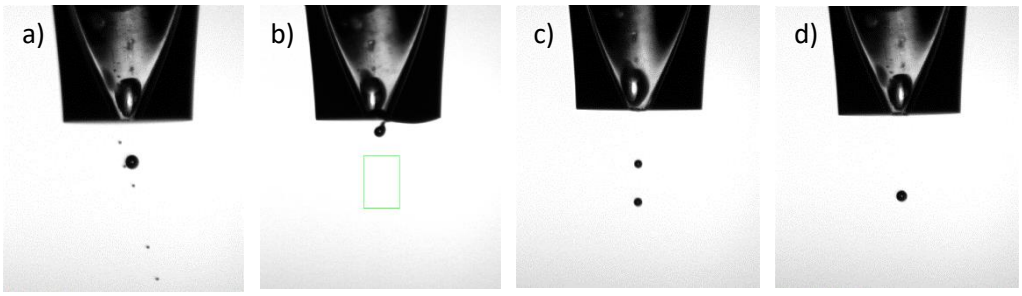

Figure I-20 Drop generation and jetting affected by printing parameters: a) nozzle cleanness, b) back pressure, c) pulse setting, and d) stable jetting.

Figure I-20 shows a captured image of a Microfab nozzle with an 80 μm diameter jetting ink in droplet form under various conditions. The most-frequently observed unreliable jetting may be due to one of three different components of the printer: the print head ejector nozzle, back pressure of the print head controlling the liquid meniscus, and wavefunction pulse generating the droplet ejection. If outside of the printer nozzle is wetted, the ejected droplet will not form correctly due to a deformation of the meniscus at the ejector orifice. The ejected ink subsequently deforms into multiple droplets which is observed as satellites (**Figure I-20.a**). Satellites disappear after the ejector orifice is cleaned and dry, allowing a more stable formation of the meniscus during the ejection process. If the printer head is not cleaned well or the inside of the ejector contains particles or dust, these contaminants also interfere with jetting, which results in undesirable ejection directions or in breaking up of ejected droplets, which is also observed as satellites. The ejector backpressure controls the meniscus as well as holds ink in the ejector, preventing leaking through the nozzle. If the backpressure is too low, the ink starts to leak out of the nozzle and forms a bulge at the nozzle tip. Usually, in this case, the volume of ink at the nozzle exit is much larger than the volume of droplets, and hence, the drop formation and jetting cannot be achieved. If only a part of nozzle tip is wet, drop jetting can be seen, but due to the non-uniform wetting at the nozzle exit, the bulge attracts drops toward it, changing the jetting direction unpredictably (**Figure I-20.b**). If the nozzle is clean and the back pressure is set properly in order to provide a stable and uniform meniscus, the pulse generation is the main factor determining drop volume and jetting speed.

The droplet can be split according to the pulse settings actuating the piezoelectric actuator for the droplet ejection (**Figure I-20.c**). In the case of multiple drop formation, no differences will be observed on printed patterns because the satellite drops will fall onto the main droplet during the printing process. However, if there is a misalignment, the satellite drops can lead to undesired printing because the drop generation is still unstable.

3. Patterning

After the pulse and the backpressure are set and the ink and the nozzle are loaded for a reliable jetting behaviour, the frequency of jetting and the spacing of drops should be controlled to print the desired pattern. The frequency is defined as a jetting speed (**Figure I-21.a**), and the spacing is the center-to-center distance between two adjacent droplets (**Figure I-21.b**). The printhead moves with a given velocity which can be calculated by multiplying the frequency and the spacing. Printing in low frequency is not desirable because the printing speed correlates with the jetting frequency. The frequency does not affect the quality of the final pattern, but it should be set within a range where the printer can jet sequentially without missing drops due to a higher frequency. The typical jetting frequency ranges from a few hundred to a thousand Hz, and 300 Hz is used in this research. However, the spacing variations may greatly affect the final printed pattern.

When printing a square pattern, assuming **Figure I-21.d** is a final pattern desired, if the overlapping between drops is negative value, the drops are not linked in the x-direction printing shown in **Figure I-21.c**. If drops do not overlapped enough, the patterned edge is not smooth in the y-direction (**Figure I-21.c**), and if the adjacent droplet overlap is too large, the ink will overflow or make a bulging making a pattern blunt [49]. The optimal spacing varies mainly by the drop diameter, the surface wettability, and the ink viscosity. In the case of printing DCB-based P3HT solution, 60% of diameter overlapping gave appropriate wetting, spreading, and smooth edge of the pattern after drying. However, the droplet spacing may be quickly adjusted by trial and error since many factors can affect the printed droplet with the Ceradrop system used in the experiments. Moreover, uniform surface morphology is

important to achieve a well-defined pattern. This result can be achieved by cleaning or SAM treatment on the surface to modify surface energy evenly.

The printing examples are shown in **Figure I-22**. A complex design with multi layers and fine features down to 5 μm can be realized once all the parameters are set within a reliable range based on the ink properties.

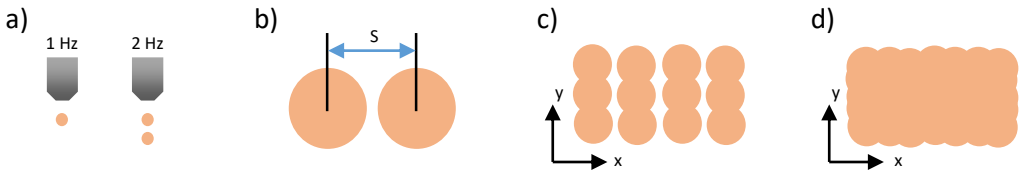

Figure I-21 Schematic illustration of a) jetting frequency, b) spacing between two droplets, c) sparsely filled-square pattern, and d) filled-square pattern.

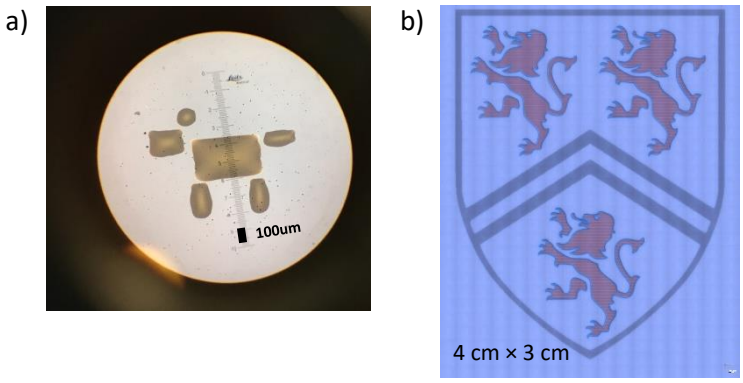

Figure I-22 a) A dog printed with AgNP ink on SiO_2 substrate features smaller than a millimeter. b) UW logo printed with model ink with three different heads: Cartridge (lions), Q-class (logo frame), and aerosol jet (outlines); features 4 cm × 3 cm.

I.5 Materials

I.5.1 Poly(3-hexylthiophene) (P3HT)

Poly(3-hexyIthiophene) (P3HT) is a representative p-type semiconducting polymer and widely investigated in the last few decades for OTFTs and light harvesting applications since it is easy to process and has high hole carrier mobility, which ranges up to 0.1 cm^2/V-s [50], [51], [52], [53], [54].

Charge transport in polymers is limited by their disordered matrix resulting in low charge-carrier mobilities. However, the crystallinity in polymers can be highly improved by molecular orientations and finally formed structures, varying by process conditions [34], [55].

P3HT has long-range intermolecular side-chain which consists of thiophene rings with 3-alkyl substituents. The 3-alkyl substituents can be oriented in different ways incorporating an adjacent thiophene ring: head-head (HH), head-tail (HT) and tail-tail (TT) (**Figure I-27**). A regioregular P3HT is composed of only HT-HT and other combinations are considered as regioirregular [56]. Thus, regioregularity stands for the percentage of HT. A two-dimensional illustration of regioregular P3HT is depicted in **Figure I-26.a**. With high regioregularity P3HT, a better ordering film with a smaller band gap and higher electroconductivity can be achieved [34], [55], [24].

In a three-dimensional view, P3HT forms inter-chain interaction as a highly ordered pi-stacked polymer which is shown in **Figure I-26.b**. To be a preferred orientation, the hexyl side chains should be normal to the substrate and the backbone, or π-stacking should be parallel to the substrate. This is a so-called edge-on orientation. On the other hand, face-on orientation has π-stacking oriented along the substrate normal (**Figure I-28**). P3HT crystal limits charge transport in <010> and <001> directions since transport through <100> direction is prevented by hexyl chains [42]. In other words, the polymer backbone and π-π stacked layer are correlated with fast transport and lamellar stacked layer shows slow interchain transport

(**Figure I-26**). Thus, to achieve high charge mobility, the P3HT film should be continuous and the P3HT molecules need a strong π-π interaction along with densely packed chains.

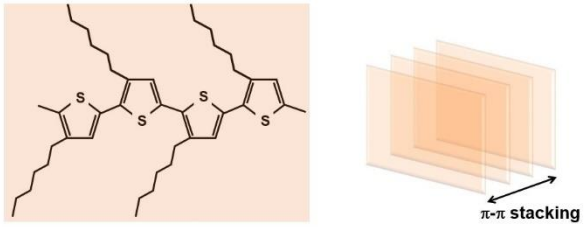

Figure I-23 Schematic of a) conjugated P3HT, and b) π- π stacking of conjugated P3HT in edge-on direction.

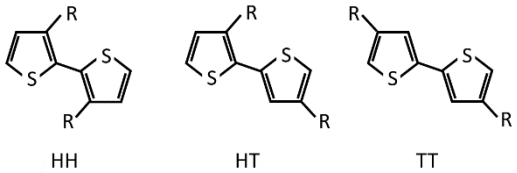

Figure I-24 Structures of possible couplings in the dimers of 3-alkylthiophene rings: head-to-head (HH), head-to-tail (HT), and tail-to-tail (TT).

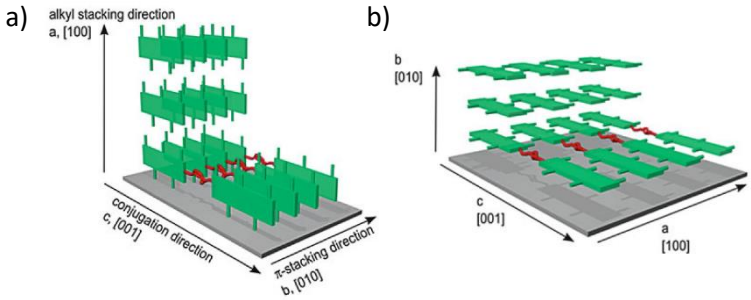

Figure I-25 Molecular orientation of P3HT in thin layers: a) edge-on orientation, and b) face-on orientation [56]. *Reprinted (adapted) with permission from (Adv Polym Sci (2014) 265: 39–82). Copyright (2014) Springer-Verlag Berlin Heidelberg.*

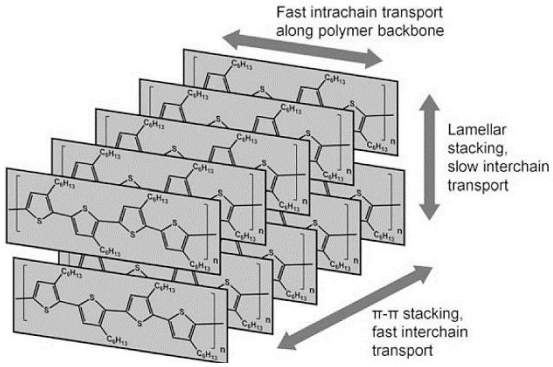

Figure I-26 Ordering of P3HT chains in crystalline aggregates and possible slow and fast charge transport directions [56]. *Reprinted (adapted) with permission from (Adv Polym Sci (2014) 265: 107–138). Copyright (2014) Springer-Verlag Berlin Heidelberg.*

I.5.2 Molybdenum disulfide (MoS_2)

Transition metal dichalcogenides materials (TMDCs) have received great attention for their high electrical performance, mechanical properties, and applicability in flexible electronics. MoS_2, a typical TMDCs, is especially suitable for electronic devices due to its intrinsic and sizable band gap properties [57].

The MoS_2 has a unique property of band gap varying with the thickness of layers. Because the conduction band minimum and the valance band maximum changes by the number of layers, the band gap changes as well with the transition of indirect to direct band gap [58]. Bulk MoS_2 is known to have an indirect band gap of ~1.2 eV [59], whereas monolayer MoS_2 has a direct band gap of ~1.9 eV [60], [61]. The reported charge carriers mobility of bulk MoS_2 is larger than 100 cm^2/V-s [62] and electron mobility of single layer MoS_2 already exceeded 200 cm^2/V-s from initial studies [58].

MoS_2 has strong molecular bonds which gives high mechanical strength and a high Young's modulus. Whereas, interlayers are connected with weak van der Waals force [58]. **Figure I-27** shows an atomic structure of vertically stacked MoS_2 layers. The hexagonal layers of Molybdenum (Mo) is sandwiched between two layers of Sulfide (S) and composed as MoS_2. Each layer of MoS_2 are coupled via van der Waals force with a single layer thickness of 6.5 Å. Stacked layers can be separated into a single or a few layers with exfoliation methods.

The exfoliation method categorizes into mechanical and chemical. Traditionally, "Scotch tape method" has been used to mechanically exfoliate bulk 2D materials into a single or few layers [62]. This gives pristine quality layers; however, the yield is very low considering the physical limitations of the method, generating flakes at most tens of micrometers [58]. For large-scale applications, aqueous exfoliation is more beneficial. The suggested method so-called chemical exfoliation has two different approaches: ion intercalation [63] and solvent-based exfoliation [64]. Ion intercalation needs an electrochemical setup which is complex and sensitive to the environment, whereas, a solvent-based method is simple and insensitive to air and water. N-methylpyrrolidone (NMP) and isopropyl alcohol (IPA) are initially introduced as organic solvents for exfoliating bulk MoS_2. The solvent-based method was further developed by mixing surfactants for a better suspension [65].

Once the layered materials are exfoliated, the changes in electrical properties open a new possibility in applications. Especially, few layer materials dispersed in solutions can be distributed as nanoparticles or formed into films. Other than exfoliating bulk MoS_2 crystals, MoS_2 nanoparticles are commercially available from several vendors in forms of powder and suspension (Sigma Aldrich, Graphene Supermarket). Still, powdered MoS_2 needs further exfoliation when solution processing, because some adjacent MoS_2 layers are stacked due to its attractive force (*i.e.* Van der Waals force).

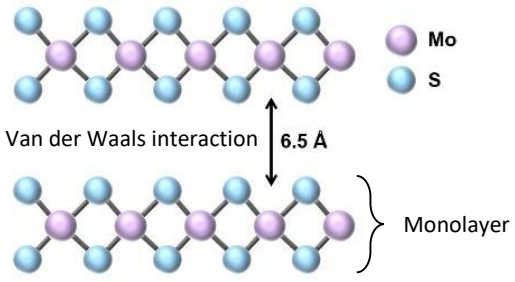

Figure I-27 Atomic structure of bi-layer MoS_2. Each monolayer of MoS_2 is coupled via weak van der Waals force between the layers and the distance is 6.5 Å.

I.6 Organic-Inorganic hybrid TFTs

I.6.1 Motivation

The solution processible polymeric semiconductors are highly disordered that results in poor field-effect mobility for TFT applications. On the other hand, inorganic materials with superior electrical performance are not applicable for large-area applications since its deposition over large areas is limited. There has been an attempt to solution process two-dimensional (2-D) materials such as graphene and single wall carbon nanotubes (SWCNTs) to fabricate electronics [9], [10], [11], [12]. However, these materials typically have metallic behaviour that results in transistors with relatively poor on/off ratios [13]. Solution-dispersed nanoparticles are neither favorable for transistors because their unconnected networks show no conductive behavior. To overcome this challenge, one approach is to reduce film disorder by bringing crystalline inorganic materials into polymers as a hybrid semiconductor composite. Through this approach, the limitations, such as low field-effect mobility and non-soluble process of both the organic and inorganic materials can be overcome. To address these problems, one suggestion is to use transition-metal dichalcogenide (TMD) semiconductors to create a mixture of inorganic-organic composite materials for TFT fabrication.

In this study, we used molybdenum disulphide (MoS_2) nano-particles as an inorganic material and poly(3-hexylthiophene) (P3HT) as an organic material. MoS_2 is a prospective candidate to be incorporated into the hybrid TFT channel material since it potentially has high field-effect mobility, good transparency, and flexibility. These unique properties are due to its atomically thin layer and two-dimensional surface. P3HT is well known for good stability, relatively high field-effect mobility, and is easy to process and handle compared to other polymeric semiconductors.

It is widely known that both MoS_2 and P3HT have favorable properties for TFT applications; however, the compatibility between two materials is important to be used as a

hybrid composite. From the energy band diagram of the device which is shown in **Figure I-28**, both the valance band edge of MoS_2 and HOMO level of P3HT can be found around 5.2 eV. This energy level match indicates the Schottky barrier height to overcome at the MoS_2-P3HT interface and the majority carrier, hole, is relatively small and thermionic transport across the barrier is expected from one material to another. Moreover, Au has a high work function of 5.1eV which matches well with the HOMO level of P3HT. We find that MoS_2 and Au have the proper energy level for hole transport and injection. In the later studies in III.3 and III.4, the work function match of Au is important as thermally deposited Au is used as electrodes for the fabricated TFTs.

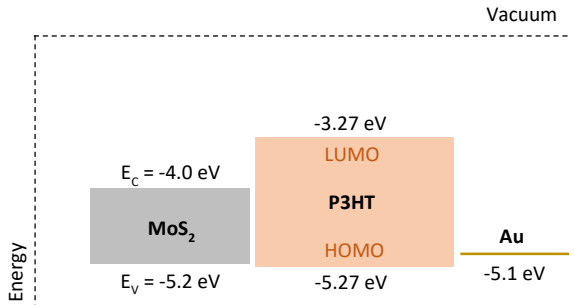

Figure I-28 The energy band diagram of MoS_2, P3HT, and gold at the interface of electrode-active layer. The energy levels show a work function of gold, an electron affinity of P3HT, and a bandgap of MoS_2.

I.6.2 Recent progress and limitations

Previous works of blending organic semiconductors with various inorganic materials such as graphene [66], [67], [68], carbon nanotubes (CNTs) [69], [70], [71], [72], tungsten disulfide (WS2) nanotubes (NTs) [73], titania (TiO2) nanorods [74], zinc oxide (ZnO) nanorods [75], and molybdenum disulfide (MoS_2) [76] are reported. Material selection, deposition method, and electrical parameters are summarized in

Table *I-1*.

They have reported a remarkable increase in field-effect mobility resulting from incorporating nanoparticles. These studies suggest that nanoparticles work as conducting

bridges within semiconductor film. However, the main challenges of these works are low on/off ratio less than three orders of magnitude [67], [70], [73], [75], and large threshold voltage shifts greater than 20 V [66], [67], [68], [69], [70], [74], [76]. Low on/off ratio is known to be affected by the percolation threshold of nanoparticles and increased coverage in the channel region. Some studies have shown that metallic tubes like CNTs can build a potential at the polymer-CNT interface. Thus, the dominant presence of CNT results in strong electrostatic interaction which generates threshold voltage shift and a high off-current in hybrid TFTs [69], [77]. Overall, the surface treatment and post-fabrication annealing process were considered important because enhancing a performance baseline FET leads to hybrid FET exhibiting better performance.

Some studies show exceptional electrical performance by obtaining high mobility with acceptable threshold voltage and on/off ratio [66], [71], [72]. This observation was attributed to well-dispersed nanoparticles in the hybrid suspension and selection of high performance polymeric semiconductors. However, most of the deposition of organic-inorganic composite inks were limited to spin-coating and there was little attempt to print the material.

Table I-1 Previously reported organic-inorganic composite TFTs organized with materials, deposition method, and device parameters.

Ref No.	Organic Semiconductor	Nano-material	Deposition method	$\mu_{sat.}$ [a)] (cm^2/V-s)	V_{TH} [a)] (V)	I_{ON}/I_{OFF} [a)]
[66]	P3HT	Graphene	spin-coating	0.17	< -20	~10^4
[66]	PQT-12	Graphene	spin-coating	0.6	~ -10	~10^5
[69]	PQTBTz-C12	SWCNT	printing	0.23	> 20	~10^7
[70]	P3HT	SWCNT	spin-coating	0.0716	< -20	< 10^3
[73]	P3HT	WS_2 NT	spin-coating	-	0.07	8.28 × 10^2
[71]	PTH	SWCNT	spin-coating	0.1	> -10	~10^4
[72]	Pentacene	CNT	evaporation	1.2	11.00	3 × 10^6
[72]	α-6T	CNT	evaporation	0.13	-1.00	1 ×10^5
[74]	P3HT	TiO_2	spin-coating	0.23	< -20	~10^5
[75]	P3HT	ZnO	spray coating	2.62 ×10^{-3}	-6.10	47.6
[67]	P3HT	Graphene	spin-coating	0.21	< -20	1.06 ×10^2
[68]	P3HT	Graphene	spin-coating	0.006	< -20	2 ×10^3
[76]	P3HT	MoS_2	spin-coating	5.09 ×10^{-2}	< -20	5.81 ×10^5

Here, we suggest a solution processible molybdenum disulphide (MoS_2) suspended in poly(3-hexylthiophene) (P3HT). The nanocomposite solution was used for an active channel layer of TFTs to fabricate a bottom gate TFT. As the solution-based approach, our hybrid ink will be applied and used to realize enhanced OTFT for printing electronics.

I.6.3 Experimental outline

An attempt to blend semiconductor polymer and nanoparticles is comparably new, and continuing efforts are being made to create reproducibly good performance. Mixing two different materials may generate unexpected variables from the materials to device level, which is difficult to control. Thereby, we suggest a two-step approach to deposit one material, nanoparticles, first and then apply a known method with another material such as a semiconducting polymer. This will allow more control over the process.

We used a two-step deposition process to fabricate back-gate MoS_2-P3HT composite TFT structures: deposition of MoS_2 followed by deposition of the P3HT polymeric semiconductor. The MoS_2 nanoparticle suspension is deposited using a drop-cast method and the finally formed MoS_2 film should be uniform in order to work as a stable channel region and also for reproducibility. The assembly of the MoS_2 nanoparticles from a suspension in liquid needs to be controlled in order to obtain a well-defined percolation network with densely packed particles. However, a major problem for assembling particles within a liquid typically results in the formation of a "coffee-ring" shape where the suspended particles form around the edge of the droplet in a discontinuous assembly through the printed area [78], [79]. This effect hinders the uniformity of the deposited material on the substrate, but the uniformity may be controlled by modifying the surface energy of the substrate [80]. After forming a MoS_2 assembly, silver source-drain electrodes and a P3HT semiconductor layer are deposited using inkjet printing. The final architecture of the active layer can be described as a P3HT film

containing MoS_2 nanoparticles, which are uniformly distributed near the semiconductor-dielectric interface.

After checking the feasibility with the two-step deposition process, a direct mixing of MoS_2 and P3HT is attempted and a hybrid ink formulation is presented. MoS_2 nanoparticles as a powder are blended into the P3HT solution to make a suspension. However, it is challenging to make a homogenous suspension due to the limitation of lab equipment; MoS_2 is not fully exfoliated into single layers and bulk material still exists [64]. This problem is addressed by using a compatible filter to remove large aggregates and obtain a more uniform suspension. While the uniformity is improved, the concentration of ink is not as well controlled due to limitations of the lab equipment for formulating the hybrid ink [81], [82]. The prepared ink is initially tested with spin-coating and then printed to realize inkjet-printed MoS_2-P3HT hybrid TFTs.

Above all these processes, before proceeding to organic-inorganic hybrid TFT, a P3HT TFT as a baseline FET is investigated and fabricated with spin-coating and printing method.

Part II P3HT thin-film transistor fabrication and characterization

II.1 Spin-coated P3HT TFTs

II.1.1 Fabrication issue of spin-coated P3HT TFTs

1. Effect of SAM and SAM materials

As discussed in I.3, the formation of self-assembly monolayer (SAM) is effectively manipulating the surface energy which further controls material deposition, wetting, and drying over the SAM treated surface. Especially in spin-coated devices, a film quality is mainly determined by an interaction at the substrate surface and the film interface. We tested an effect of two different SAM materials, dodecyltrichlorosilane (DDTS) and hexamethyldisilazane (HMDS), on the SiO_2 surface. DDTS is known for its long alkyl chain length which gives high hydrophobicity to the surface and HMDS is one of the most commonly used SAM material for surface modification in various applications [83], [27].

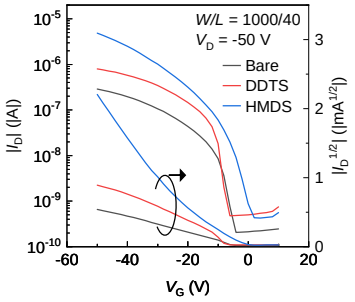

Table II-1 Device parameters of P3HT TFTs fabricated on a bare, DDTS-treated, and HMDS-treated substrate.

	$\mu_{sat.}$ (cm^2/V-s)	V_{TH} (V)	*S.S* (V/dec.)
Bare	3.00×10^{-4}	0.07	-7.81
DDTS	6.00×10^{-4}	7.37	-7.55
HMDS	8.70×10^{-3}	-14.26	-6.81

Figure II-1 Transfer characteristics of P3HT TFTs fabricated on a bare, DDTS-treated, and HMDS-treated substrate in logarithmic scale (left axis) and square root (right axis).

To investigate the effect of SAM treatment on the electrical performance of devices, solution-cleaned wafers with patterned Au electrodes are prepared and immersed in the SAM solution. In the case of DDTS, the substrate was immersed for 30 min and for HMDS, the substrate was immersed for 12 hr. The given time was a general treatment time for each SAM material. The wafers are then rinsed with toluene and blow-dried with nitrogen. The P3HT was spin-coated following the general procedure introduced in I.3. The results shown in **Figure II-1** and **Table II-1** indicate that SAM treatment enhances electrical performance in terms of on-current and mobility. The bare device which is not treated with SAM has a mobility of 3.0×10^{-4} $cm^2/V\text{-}s$; whereas, SAM treated devices show higher mobility compared to the bare device, 6.0×10^{-4} $cm^2/V\text{-}s$ for DDTS-treated device and 8.7×10^{-3} $cm^2/V\text{-}s$ for HMDS-treated device. The device dimensions were W = 1000 μm and L = 40 μm. The devices were measured at V_D = -50 V, where the transistor operates in the saturation region. The result suggests that the HMDS SAM layer formulated on the oxide surface actually improves the electrical characteristics of TFTs. This improvement may be attributed to better crystallization of P3HT at the dielectric surface-polymer interface of SAM treated samples as discussed in I.3.

Better performance of HMDS treated device compared to DDTS treated device can be explained with the length of alkyl chain. DDTS have 12 carbon atoms (C) dangling; whereas, HMDS has very short chain of $Si(CH_3)_3$ after displacing with hydroxyl groups (-OH) on SiO_2 surface. The chains of SAMs are canted which can create tilt-order phase transitions and cause defects in itself [22]. In other words, a longer chain has more chance to be bent and possibly result in misalignment of a functional tail. Thus, the semiconducting film formation on DDTS treated surface does not reach a certain level of crystallinity due to the effect of long alkyl chains [83]. From this experiment and results, we decided to use HMDS for the SAM treatment for the Au patterned SiO_2 substrate.

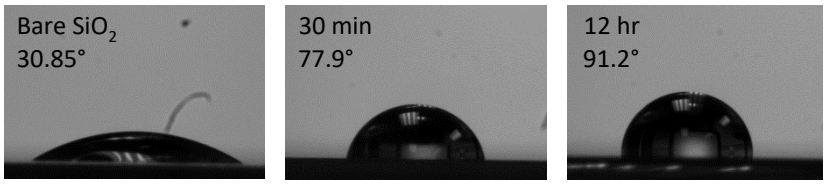

Figure II-2 Contact angle measurements of DI water droplets on HMDS-treated SiO_2 surface for different time lengths: 30.8° on bare surface; 77.9° for 30 min immersing; 91.2° for 12 hr immersing.

2. Effect of SAM treatment time

The next aspect to consider is an optimal SAM treatment time. From the contact angle measurement shown in **Figure II-2**. The average contact angle of DI water droplets on the bare SiO_2 substrate was 30.85°, indicating a hydrophilic surface. After HMDS treatment, the contact angle increased to 77.9° for a 30 minute treated surface and 91.2° for a 12 hr treated surface. This result indicates that the HMDS treatment actually makes the SiO_2 surface more hydrophobic. Moreover, the surface treated longer time shows bigger contact angles and this is because an extended immersion time increases the SAM coverage of the surface. If the treatment time is not enough, the chemical characteristics of a surface will be not uniform, and this could give large variations to devices fabricated at the same time [22]. However, in the case of DDTS, increasing the immersion time does not change the surface properties. A high contact angle of 109.6° is observed in 30 min treated samples and a little reduced contact angle of 97.7° is observed in 12 hr treated samples. Therefore, DDTS treatment is more applicable for samples which need short time treatment and a high hydrophobicity. Nonetheless, the high hydrophobicity does not proportionally correlate with the improved TFT performance shown in **Figure II-1** and **Table II-1**.

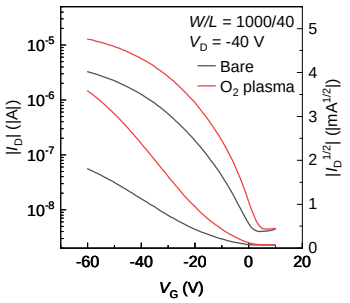

Table II-2 Device parameters of P3HT TFTs fabricated on a bare, and an oxgen plasma-cleaned substrates immersed in HMDS for 1 hr.

	$\mu_{sat.}$ (cm^2/V-s)	V_{TH} (V)	*S.S* (V/dec.)
Bare	3.20×10^{-3}	-10.05	-13.32
O_2 plasma	1.29×10^{-2}	-8.08	-10.03

Figure II-3 Transfer characteristics of P3HT TFTs fabricated on a bare, and an oxgen plasma-cleaned substrates immersed in HMDS for 1 hr in logarithmic scale (left axis) and square root (right axis).

3. Effect of plasma cleaning

Enhancing the efficacy of the SAM attachment to the surface is desirable in order to reduce the surface functionalization process time. In order to minimize the time for the SAM to attach onto the substrate, the cleanliness of the surface is an important consideration because surface contaminants and residues can act as extrinsic defects to the SAM [22]. Here, an oxygen plasma as a dry cleaning method was introduced to clean the surface. The plasma cleaning can remove strongly attached or chemically bonded organics on the surface which mechanical sonication and wet cleaning methods using organic solvents cannot remove [21]. The plasma cleaning is a very simple process that Au patterned wafer radiated by oxygen plasma for 2 min in a vacuum chamber. The SiO_2 substrates are then immersed in HMDS for 1 hr as an effort to reduce SAM treatment time. From the literature, during the varied treatment time from 30 min to 16 hr, the water contact angle saturated by treating over 1 hr on dry-cleaned surfaces [84]. **Figure II-3** and **Table II-2** show the result plasma cleaning improving overall electrical characteristics. The mobility was increased by almost one order of magnitude from 3.20×10^{-3} cm^2/V-s to 1.29×10^{-2} cm^2/V-s after the plasma cleaning, keeping a threshold voltage in a similar range. Comparing with a 12 hr immersion sample with the mobility of 8.7×10^{-3} cm^2/V-s (**Table II-1**), 1 hr immersion sample with plasma-cleaned surface showed even higher

mobility. This implies the oxygen plasma removed residues on the surface effectively, and as a result, the SAM coverage improved in a comparatively short time.

From the investigation of SAM treatment time and the effect of surface cleaning, we concluded that 1 hr immersion in HMDS after O_2 plasma cleaning is efficient in process time and reliable without giving many variations to the device performance.

II.1.2 Spin-coated device fabrication process

The fabrication of bottom-gate bottom-contact TFT devices with a spin-coated P3HT channel layer followed OTFT processing described in I.3.

The organic polymer, poly(3-hexylthiophene) (P3HT) (95.7 % regioregularity, Ossila), was dissolved in 1,2-dichlorobenzene (Sigma-Aldrich) while the solution was heated to 85 °C for 1 hr on a hotplate. The concentration of P3HT solution was 10 mg/ml. The solution was prepared in N_2 condition, avoided exposure to UV light and used shortly after prepared.

Highly doped p-type silicon substrates were used as the common bottom gate structure with thermally grown 100 nm thickness silicon dioxide as a dielectric layer. The source and drain electrodes were patterned by conventional photolithography and 2 nm Cr as an attachment layer and 40 nm Au as a charge injection layer was thermally deposited. The channel dimension of the device was 1000 μm in width and 30 μm in length.

Prepared patterned substrates were cleaned with Isopropyl alcohol, acetone, and deionized water sequentially then treated with oxygen plasma to remove possible remaining organics. HMDS was used as a SAM material to improve the molecular ordering of the polymer thin film formation and to control the wettability of SiO_2 and Au by modifying surface energies.

The P3HT film was spin-coated on the HMDS-treated surface at 3000 rpm for 80 s (using an acceleration of 800 rpm/s) under nitrogen condition. The devices were then oven-annealed in a vacuum for 1 hr at the ramped up temperature from room temperature to 120 °C. Finally,

the fabricated devices were characterized as pulsed in the current and voltage (I-V) measurement using a Keithley 2400 under vacuum and dark conditions.

II.1.3 Spin-coated TFT device electrical measurements and characterization

The transfer characteristics of spin-coated P3HT TFTs is plotted as **Figure II-4.a**, with drain current (I_D) as a function of gate voltage (V_G), I_D-V_G, at a constant drain voltage (V_D) of −40 V.

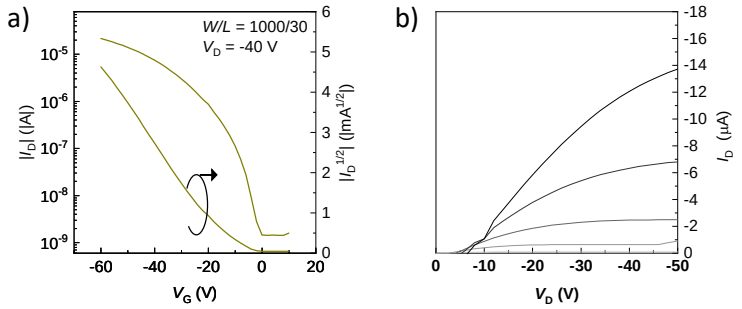

Figure II-4 a) Transfer characteristics of spin-coated P3HT TFTs in logarithmic scale (left axis) and square root (right axis). b) I_D-V_D of spin-coated P3HT TFTs.

Table II-3 Device parameters of spin-coated P3HT TFTs.

$\mu_{sat.}$[a)] (cm^2/V-s)	V_{TH}[a)] (V)	$S.S$[a)] (V/dec.)	I_{ON}/I_{OFF}[a)]
(9.74 ± 5.32) × 10^{-3}	-14.28 ± 2.01	-5.42 ± 0.50	(9.97 ± 4.24) × 10^3

[a)] average of 9 devices

The hole field-effect mobility of each device in the saturation regime was calculated by the gradual-channel approximation. The threshold voltage, V_T, was determined using a linear fit to the square root of drain current versus gate voltage. These calculated values are summarized in **Table II-3** by averaging 9 devices. The average field-effect mobility of spin-coated P3HT TFT is 9.74×10^{-3} cm^2/V-s with a deviation of 5.32×10^{-3} cm^2/V-s. The spin-coated film uniformity or the thickness can vary a little from the center to the edge and this may cause deviations on devices fabricated on the same die. The maximum mobility is 1.88×10^{-2}

cm^2/V-s which is comparable with previously reported spin-coated P3HT TFTs [74], [67]. The measured on/off ratio is 9.97×10^3, which is comparably low for P3HT TFTs, is due to limitations of our measurement setup as described in I.3. An on/off ratio up to 10^6 could be achieved if measured with the picoammeter based on our previously dc-measured devices.

The output characteristics of a spin-coated P3HT TFT are shown in **Figure II-4.b**. The drain current was measured as a function of drain voltage (V_D) with different gate bias voltages (V_G) under dark conditions. The range of drain bias voltages was swept from 0 V to -50 V in steps of -2 V. The output curve depicts the modulated drain current by an applied drain voltage. The output characteristics showed good saturation behaviour with well-defined saturation currents. However, the drain current does not flow near the zero drain voltage. This shift in drain current indicates that barriers exist when charges are injected from the s/d electrodes into the channel. The quality of source-drain electrodes or the film quality at the electrode-semiconductor interface are possible factors. This will be investigated under future work.

II.2 Inkjet-printed P3HT TFT

II.2.1 Inkjet-printed TFTs

Initially, P3HT TFTs were fabricated using an inkjet printing method, by printing source-drain electrodes and a semiconductor film. The general fabricating procedure follows the OTFT processing introduced in section I.3, especially, **Figure I-9**. A highly doped silicon substrate with an oxide layer was solution-cleaned. Silver nanoparticle (AgNP) ink was ejected through a multi-nozzle cartridge printhead following the pre-designed electrode patterns. The printed AgNP electrodes were then sintered at 200 ℃ for 30 min on a hotplate in nitrogen condition. The patterned substrate was treated with SAM, then P3HT solution was applied using a Microfab single nozzle along the channel region. The device was then annealed at 130 ℃ for 1 hr on a hotplate in nitrogen condition. This inkjet-printed P3HT TFT with AgNP electrodes will hereafter be referred to as an all-printed TFT.

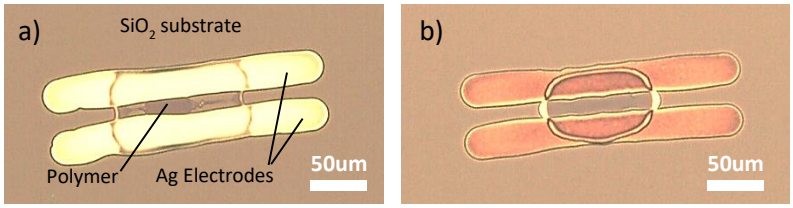

Figure II-5 P3HT printed on top of AgNP electrodes on a) bare surface, and b) DDTS-treated surface.

1. Surface modification

Surface modification is important for film crystallization and also for controlling the wettability of substrates. In multi layer printing, the wettability should be considered in order to print well-defined features. In **Figure II-5.a**, the polymer was supposed to be printed along the channel region between the silver electrodes. However, due to a surface energy difference between the SiO_2 substrate and silver electrodes, the polymer tends to wet the silver more

than the SiO_2. Polymer initially deposited on the channel region rapidly flows onto the silver. As a result, the polymer film has a vacancy in the channel region. The dark region in the channel of **Figure II-5.a** is where the film is formed, and the bright region with the same color of SiO2 substrate is where the film is not formed. Silicon oxide and silver electrodes were treated with SAM in order to reduce the surface energy difference. Oxygen plasma is not applicable due to the possible oxidization of silver electrodes. Hence, DDTS was chosen as the SAM for its effectiveness in short treatment time as discussed in II.1.1. After the surface modification, as seen in **Figure II-5.a**, the polymer wet both the SiO_2 substrate and silver electrodes uniformly. Uniform film formation gives predictable device fabrication and reliable device performance.

2. Jetting control

Figure II-6.a shows the printed droplets on a SiO_2 substrate for uncontrolled polymer printing features with offsets and satellites. The polymer is supposed to be printed between two silver electrodes as an active layer. However, in the case of uncontrolled jetting discussed in I.4.2 (**Figure I-20**), the polymer has a high chance to be jetted at unexpected times and printing occurs in undesired positions which results in a random pattern. Multiple drop jetting also has a chance to print undesirable patterns. With controlled jetting, we achieved a well-organized pattern with polymers printed exactly on the channel region without offsets or satellites (**Figure II-6.b)**.

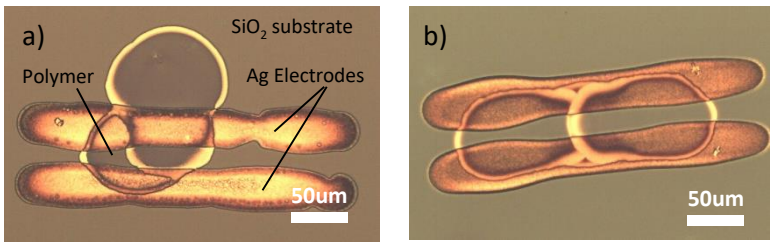

Figure II-6 P3HT printed on top of AgNP electrodes with a) instable jetting conditions, and b) stable jetting conditions.

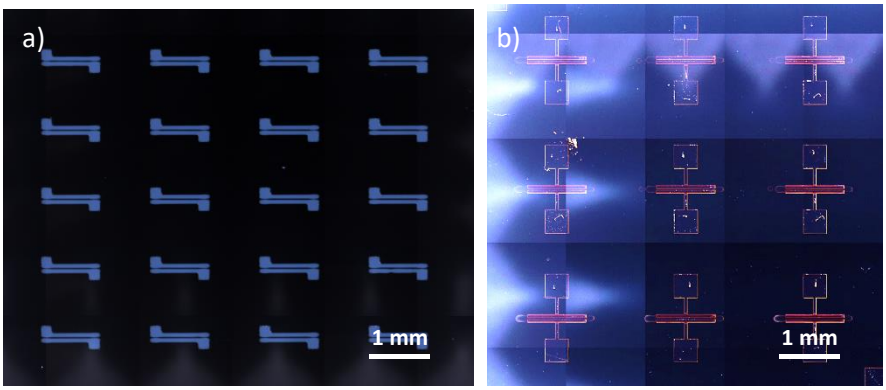

Figure II-7 a) Electrodes array printed with conductive ink on rigid substrate. b) P3HT semiconducting layer printed as an array on top of Au electrode-patterned substrate.

3. Printing parameters

In addition to achieving the correct print head driving conditions, printing parameters must be precisely controlled to achieve optimized printed features. As a result, we created a silver electrode array with the finest channel length ~ 10 μm (**Figure II-6.a**) and positioned a polymer channel array exactly on the channel region of pre-patterned Au electrodes without any offset (**Figure II-6.b**). To achieve accurate placement of the droplets onto a pre-patterned surface, fine-feature printing requires an accurate drop spacing control. Because different materials have different wettabilities and viscosities that also can be affected by the surface energy of the substrate, knowing the drop diameter is essential in designing patterns but at the same time, the actual printing and revising help ensure the desired printing quality. Layer printing requires print head offset corrections. In order to stack a layer on a pre-patterned layer, the exact positioning is essential, especially for micron-size device fabrication. A few micrometer offset can lead to a misalignment that causes device failure. Offsets can be fixed from the printer software by checking the origin manually, testing the printing, and resetting the parameters.

However, to isolate the process development to only the semiconducting polymer, and the processes to optimize the printing process conditions, we decided to use thermally evaporated Au electrodes instead of printed Ag electrodes. Au is well known for its air

stability, and thermally deposited electrodes have a uniform morphology with controlled thickness. Ag electrodes, however, need to be investigated in terms of the relation between concentration and thickness, the surface quality that might affect both film quality and the charge injection.

Table II-4 Device parameters of printed P3HT TFTs with various jetting frequency.

Frequency (Hz)	$\mu_{sat.}$ [a)] (cm^2/V-s)	V_{TH} [a)] (V)	*S.S* [a)] (V/dec.)
1	1.66×10^{-2}	-8.94	-6.98
10	1.01×10^{-2}	-9.76	-7.24
50	9.80×10^{-3}	-8.74	-7.43
300	1.64×10^{-2}	-9.80	-7.52
1000	1.35×10^{-2}	-13.05	-7.72

a) average of 3 devices

Table II-5 Device parameters of printed P3HT TFTs with various spacing between neighbor droplets.

Spacing (μm)	$\mu_{sat.}$ [a)] (cm^2/V-s)	V_{TH} [a)] (V)	*S.S* [a)] (V/dec.)
60	1.11×10^{-2}	-10.33	-7.13
80	1.26×10^{-2}	-11.17	-7.34
100	1.18×10^{-2}	-11.00	-7.39

a) average of 3 devices

To optimize the printing parameters, the jetting frequency and sequential printed drop spacing parameters were varied and the electrical performances of fabricated devices measured as a function of this variation. P3HT was printed on thermally evaporated Au electrodes on a SiO_2 substrate. The frequency of jetting varied from 1, 10, 50, 300, to 1000 Hz. Devices fabricated with either 1 Hz and 300 Hz show relatively higher field-effect mobilities of 1.66×10^{-2} cm^2/V-s and 1.64×10^{-2} cm^2/V-s, respectively (**Table II-4**). The difference between the highest and the lowest mobility was 6.8×10^{-3} cm^2/V-s, which is not significant. Threshold voltages are also in a similar range of less than 1 V except at 1000 Hz. However, major factors affecting the threshold voltage are the semiconductor-insulator interface and trap states in the

semiconductor. Thus, the frequency of jetting does not have a large impact on threshold voltage changes, and the threshold voltage of 1000 Hz might be affected by a minor difference in other device process conditions.

To investigate these other parameters, the spacing between sequentially printed drops is varied from 60, 80, to 100 μm. Field-effect mobility, threshold voltage, and subthreshold swing are noted in **Table II-5**. All the parameters are within a similar range, which means a minor change in spacing also does not much affect the film formation. However, if the spacing becomes larger than 100 μm, the drops are not continuously linked into one solid film, due to lack of material. The results show that frequency and spacing do not much affect device performance.

Among the various conditions, 300 Hz frequency and 80 μm spacing are chosen for printing P3HT solution. At 300 Hz jetting frequency, the fabricated devices showed relatively high mobility. More importantly, if the jetting frequency goes lower, the printing speed become slower which is inefficient in a sense of fabrication process, and too high jetting frequency may result in unstable jetting. With 80 μm spacing, printed droplets are packed enough to make continuous line without overflowing materials.

4. Ink formulation and processes for printed TFTs

Spin-coating and printing are different deposition methods, and they have different conditions that fit their own characteristics. For example, a P3HT concentration for spin-coating was determined experimentally regarding spin-coating speed and final thickness of the film. However, a printer deposits P3HT solution directly on the channel with controlled volumes and shapes. Therefore, the thickness can differ with spin-coating, even with the same concentration of a solution. To identify the optimal P3HT concentration for printing, we tested printed P3HT TFTs fabricated with 5 mg/ml and 10 mg/ml P3HT solution. Au electrodes were thermally deposited on silicon dioxide, and P3HT solution was printed on the channel region. **Table II-6** compares field-effect mobility, threshold voltage, and subthreshold swing of printed TFTs fabricated with 5 mg/ml and 10 mg/ml P3HT solution. The electrical

characteristics of the spin-coated TFTs are also provided for the comparison. The field-effect mobility of the 5 mg/ml device is higher than that of the 10 mg/ml device and comparable with the spin-coated device. Furthermore, **Figure II-8** shows the range of mobility, threshold voltage, and subthreshold swing. Empirically, the overall deviations of the 5 mg/ml device are smaller than those of the 10 mg/ml device, which means a film printed with 5 mg/ml solution is more uniform with more predictable performance. For this reason, 5 mg/ml has been chosen for printing in the future.

Table II-6 Device parameters of P3HT TFTs fabricated via spin-coated and printed with different P3HT solution concentrations of 10 mg/ml and 5 mg/ml.

	Conc. (mg/ml)	$\mu_{sat.}$ [a)] (cm^2/V-s)	V_{TH} [a)] (V)	$S.S$ [a)] (V/dec.)	I_{ON}/I_{OFF} [a)]
Spincoating	10	$(9.74 \pm 5.32) \times 10^{-3}$	-14.28 ± 2.01	-5.42 ± 0.50	$(9.97 \pm 4.24) \times 10^3$
Printing	10	$(5.25 \pm 4.47) \times 10^{-3}$	-6.82 ± 2.20	-7.97 ± 0.91	$(9.49 \pm 8.16) \times 10^3$
	5	$(9.80 \pm 2.30) \times 10^{-3}$	-10.25 ± 1.52	-6.09 ± 0.24	$(1.37 \pm 0.31) \times 10^4$

a) average of 6-13 devices

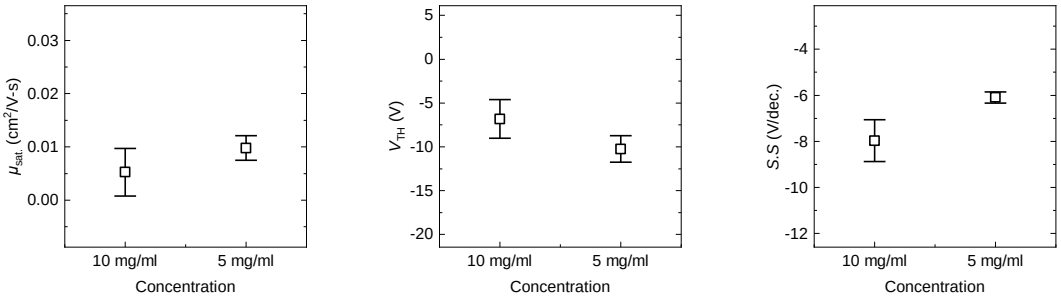

Figure II-8 Device parameters distributions of printed P3HT TFTs fabricated with different P3HT solution concentrations of 10 mg/ml and 5 mg/ml.

5. Post-processing

Semiconductor film quality is the main factor determining the performance of TFTs. The crystallization of the film and its quality is affected by the whole process, including substrate

preparation, ink formulation, deposition method (spin-coating or printing), and thermal annealing. Among the processes, the effect of annealing is investigated focused on comparing hotplate and oven annealing. Hotplate annealed devices were heated in a nitrogen ambient, at 80 °C for 20 min and at 130 °C for 20 min sequentially, and then slow cooled for 20 min. Oven annealed devices were annealed in a vacuum, with a slow ramp up from room temperature to 130 °C for 1 hour. **Figure II-9** shows an I_D-V_G plot of hot plate annealed and oven annealed devices at V_D = −40 V. The extracted parameters of field-effect mobility, threshold voltage, subthreshold swing, and the on/off ratio of 5 to 6 devices and deviations are noted in **Table II-7**. The mobility of oven annealed devices was 1.49×10^{-2} cm²/V-s, which is twice bigger than the mobility of hotplate annealed devices, 6.56×10^{-3} cm²/V-s. The deviations of oven annealed devices were smaller than those of hotplate annealed devices. Oven annealed devices show a smaller threshold voltage and higher on/off ratio, suggesting this approach produces better electrical device performance. In the case of hotplate annealing, the bottom of the device contacts with the heating source and the top exposed to air. The temperature gradient induced from the bottom to top, which may hinder the uniform formation of a semiconductor film. However, the device annealed in the oven surrounded by heated air with uniform temperature resulted in more uniform films [85].

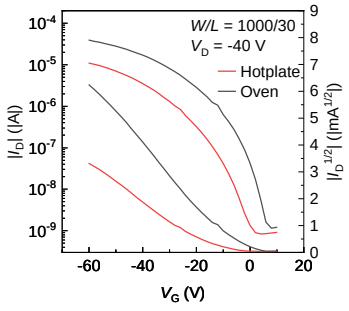

Figure II-9 Transfer characteristics of printed P3HT TFTs with the film annealed on hotplate and oven in logarithmic scale (left axis) and square root (right axis).

Table II-7 Device parameters of printed P3HT TFTs with the film annealed on hotplate and oven.

Annealing	$\mu_{sat.}$ [a)] (cm^2/V-s)	V_{TH} [a)] (V)	$S.S$ [a)] (V/dec.)	I_{ON}/I_{OFF} [a)]
Hotplate	$(6.56 \pm 2.84) \times 10^{-3}$	-15.37 ± 1.30	-10.37 ± 4.10	$(6.48 \pm 4.37) \times 10^{3}$
Oven	$(1.49 \pm 0.60) \times 10^{-2}$	-9.75 ± 2.02	-6.77 ± 0.84	$(1.05 \pm 0.40) \times 10^{4}$

a) average of 6 devices

II.2.2 Printed TFT device fabrication process

The fabrication of bottom-gate bottom-contact TFT devices with a printed P3HT channel layer follows OTFT processing described in I.3.

The organic polymer, P3HT (95.7 % regioregularity, Ossila), was dissolved in 1,2-dichlorobenzene (Sigma-Aldrich) while the solution was heated to 85 °C for 1 hr on a hotplate. The concentration of P3HT solution was 5 mg/ml, selected based on the discussion in II.2.1 (**Table II-6**). The solution was prepared in N_2 condition, avoiding exposure to UV light. All processes, from solution preparation to wafer preparation, are the same as in II.1.2, and only the active layer is deposited by inkjet printing. The prepared solution was exposed to air while printing, but this process took under 2 hrs to minimize the air exposure time.

Highly doped p-type silicon substrates were used as the common bottom gate structure with thermally grown 100 nm thickness silicon dioxide as a dielectric layer. The source and drain electrodes consisted of 2 nm Cr as an adhesion layer and 40 nm Au as a charge injection layer was thermally evaporated and patterned by conventional photolithography. The channel dimension of the device was 1000 μm in width and 30 μm in length.

Prepared patterned substrates were cleaned with Isopropyl alcohol, acetone, and deionized water sequentially then treated with oxygen plasma to remove possible remaining organics on the surface. HMDS was used as a SAM material to improve the molecular ordering of the polymer thin film formation and to control the wettability on the SiO_2 and Au surface by modifying their surface energies.

P3HT solution was printed using a Microfab single nozzle with 80 μm nozzle diameter. The drop volume was ~90 pl, and the drop diameter of P3HT printed on the prepared substrate was ~130 μm. The spacing should be controlled based on the drop diameter, and in this experiment, it was set to make a 60 % drop overlap between neighboring droplets. This overlap gave appropriate wetting, spreading, and smooth edge of the pattern after drying. The patterns were printed with 80 μm spacing, at a 300 Hz jetting frequency. A single line of 1200 μm width and 130 μm length was printed as an active layer on 9 devices consecutively.

The devices were then oven-annealed in a vacuum for 1 hr from room temperature to 120 °C. Finally, the fabricated devices were characterized as pulsed in the current and voltage (I-V) measurement using a Keithley 2400 under vacuum and dark conditions.

II.2.3 Printed TFT device measurements and characterization

The transfer characteristics of printed P3HT TFTs is plotted as **Figure II-9.a**, with drain current (I_D) as a function of gate voltage (V_G), I_D-V_G, at a constant drain voltage (V_D) of −40 V.

The hole field-effect mobility of each device in the saturation regime was extracted using the gradual-channel approximation. The threshold voltage, V_T, was determined using a linear fit to the square root of the drain current versus gate voltage. These calculated values are summarized in **Table II-8** by averaging 6 devices. The average field-effect mobility of printed P3HT TFT is 1.49×10^{-2} $cm^2/V\text{-}s$ with a deviation of 0.60×10^{-3} $cm^2/V\text{-}s$. The maximum mobility was 2.67×10^{-2} $cm^2/V\text{-}s$, highly exceeding previously reported printed P3HT TFTs with typical mobilities of 10^{-3} $cm^2/V\text{-}s$ [86], [44]. The on/off ratio is 1.05×10^4, which is comparable with other studies. Still, an on/off ratio up to 10^6 could be achieved when measured with the picoammeter based on our previously dc-measured devices.

The output characteristics of printed P3HT TFT are shown in **Figure II-9.b**. The drain current was measured as a function of drain voltage (V_D) with different gate bias voltages (V_G) under dark conditions. The drain bias voltages ranged from 0 V to -50 V in a step of -2 V. The

output curve depicts the drain current modulated by an applied drain voltage. The output characteristics showed good saturation behaviour with clear saturation currents. The device switched on nicely around $V_G = 0$ V; however, $V_D = -50$ V shows an anomalous wrinkle in the linear regime, but since other drain voltages showing linear increment at low V_G, it is attribute to a measurement tool issue. The linear I_D-V_D characteristic in the linear regime indicates that these devices are unaffected by source-drain contact resistance.

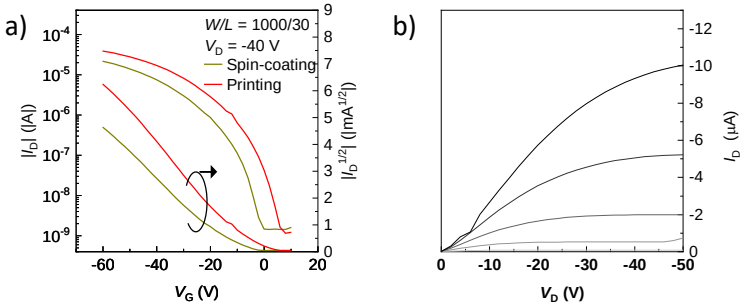

Figure II-10 a) Transfer characteristics of P3HT TFTs fabricated via spin-coating and printing in logarithmic scale (left axis) and square root (right axis). b) I_D-V_D of printed P3HT TFTs.

Table II-8 Device parameters of P3HT TFTs fabricated via spin-coating and printing.

	μ_{max} (cm^2/V-s)	$\mu_{sat.}$ [a)] (cm^2/V-s)	V_{TH} [a)] (V)	$S.S$ [a)] (V/dec.)	I_{ON}/I_{OFF} [a)]
Spin-coating	1.88×10^{-2}	$(9.74 \pm 5.32) \times 10^{-3}$	-14.28 ± 2.01	-5.42 ± 0.50	$(9.97 \pm 4.24) \times 10^{3}$
Printing	2.67×10^{-2}	$(1.49 \pm 0.60) \times 10^{-2}$	-9.75 ± 2.02	-6.77 ± 0.84	$(1.05 \pm 0.40) \times 10^{4}$

a) average of 6-9 devices

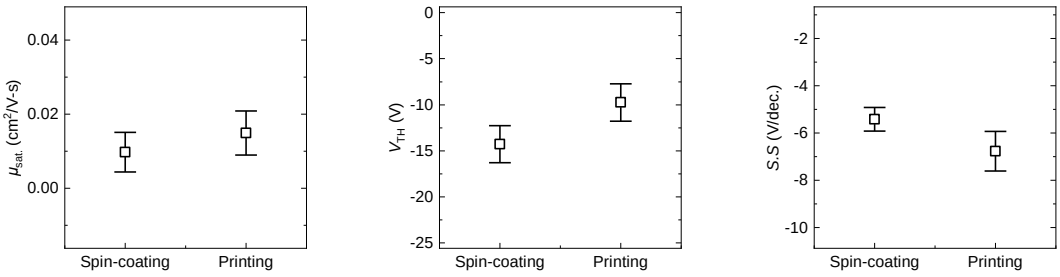

Figure II-11 Device parameters distributions of P3HT TFTs fabricated via spin-coating and printing.

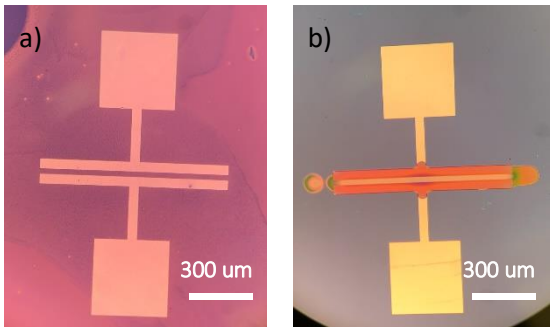

Figure II-12 Optical microscope image of a) spin-coated P3HT TFTs, and b) printed P3HT TFTs with the device dimension of W = 1000 μm and L = 30 μm.

II.2.4 Comparison with spin-coated device and analysis

The spin-coated P3HT TFTs and printed P3HT TFTs are compared in terms of electrical characteristics. The compared spin-coated P3HT TFTs results are discussed in II.1.3 and all the parameters are brought to **Table II-8**.

Figure II-9.a shows transfer curves comparing spin-coated and printed devices, and **Table II-8** summarizes key parameters and deviations from the average values. Printed P3HT TFTs show better electrical performance than spin-coated P3HT TFTs overall, with higher field-effect mobility in 1.49×10^{-2} $cm^2/V\text{-}s$ compared to 9.74×10^{-3} $cm^2/V\text{-}s$ of spin-coated devices, and lower threshold voltage by 5 V. The comparison can be also seen from **Figure II-10**, which depicts the deviation of mobility, threshold voltage, and subthreshold swing. However, the on/off ratio were not measured precisely due to limitations in the measurement tool, making it hard to say whether printed devices have a higher on/off ratio.

Figure II-11 shows optical microscope image views of spin-coated and printed P3HT TFTs. The orange film shown is P3HT deposited as an active layer in both devices. For spin-coated devices, the P3HT film covers the whole surface because the material is drop casted and then spun to coat the surface globally. The channel regions are isolated by scratching the film outside the channel region to avoid current leaking when electrical characteristics are

measured. In the case of printed P3HT TFTs, P3HT solution is deposited exactly on the channel region, which saves material and the no need to isolate devices. The Au electrodes pattern with a 30 μm channel length perfectly fits for printed P3HT film considering the width of the printed P3HT line ~130 μm. Due to the hydrophobicity of the SiO_2 substrate, P3HT solution tends not to overflow into the SiO_2. Rather it stays within the Au source-drain, enabling thick enough P3HT film to be formed along the channel region, thus giving a fairly good performance. If the channel is narrower, a part of the P3HT ink flows through the Au bridge connecting the source-drain to the measurement pads. This makes a thinner P3HT film adjacent to the bridge due to missing solution and lowers the performance. If the channel is larger, the Au source-drain is not fully covered, and P3HT solution pinned randomly on the Au source-drain, which can affect the thickness of the finally formed film.

Part III MoS_2-P3HT hybrid channel TFT

III.1 Inkjet-printed P3HT TFT on MoS_2 assembly

III.1.1 MoS_2 assembly

As discussed in I.5.1, molybdenum disulphide (MoS_2) is introduced to TFT applications for its superb electrical characteristics. MoS_2 in a nanoparticle form is solution-processed for further incorporation with solution-based polymeric semiconductors and printing applications. Solution-based MoS_2 nanoparticles are commercially available and simply can be prepared in a lab as well. MoS_2 nanoparticles can be deposited as a thin-film; yet, all the particles are unconnected. Single or a few layer MoS_2 itself shows semiconducting behaviour [87], [58], but no devices showing clear switching behaviour solely has been demonstrated by devices composed of nanoparticles [88], [11], [12]. Herein, we suggest to fill vacancies of MoS_2 film with semiconducting polymers to connect the MoS_2 particles, and make it as an organic-inorganic hybrid semiconducting film. For testing the semiconducting behaviour of the polymer-MoS_2 composite film, the device structure is proposed as **Figure III-1**. MoS_2 nanoparticles are drop-casted on a SiO_2 substrate first, then Ag electrodes and a P3HT semiconducting layer are printed sequentially.

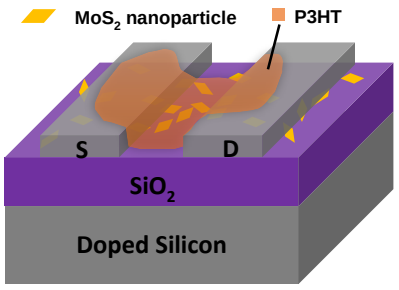

Figure III-1 Schematic device structure of a MoS_2-P3HT composite channel TFT with a bottom-gate, bottom-contacts structure. The AgNP electrodes and P3HT film is printed on MoS_2 assembly.

To fabricate the suggested TFT device structure, it is important to achieve a uniform and dense assembly of MoS_2 nanoparticles on the substrate surface by suppressing the coffee-ring effect. The coffee-ring effect is observed due to the different rate of solvent evaporation on the edge and the center of a droplet. Once the contact line is pinned, the edge dries fast and fluid flows from the center to the edge making a gradient in the material density [89], [48].

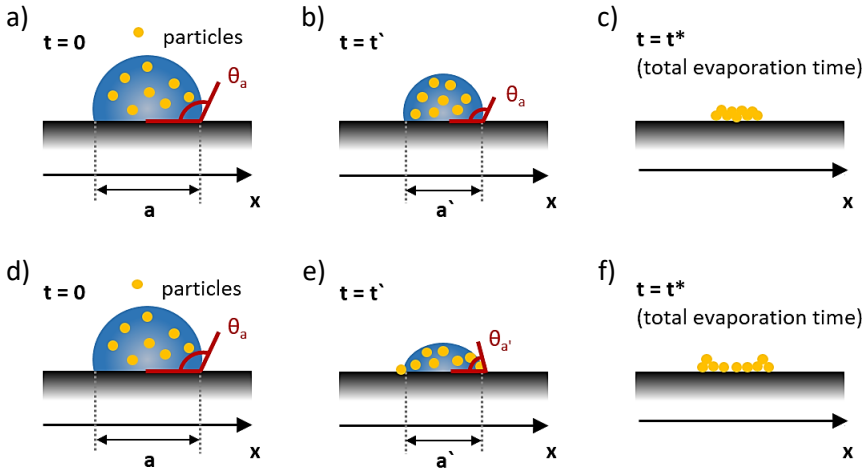

Figure III-2 Schematic illustration of the evaporation dynamics of nanoparticles suspended in a droplet on a hydrophobic surface ((a)-(c)), and a hydrophilic surface ((d)-(f)).

Figure III-2 schematically demonstrates the evaporation characteristics of a droplet containing suspended MoS_2 particles. In order to suppress the coffee-ring effect, the advancing and receding contact angle of the droplet must remain the same over time from the initial droplet formation time (t = 0) to the removal of the liquid by evaporation (t = t*). If the contact angle remains the same, the radius of curvature stays the same as well. The particles inside the droplet are distributed with the same gradient. During this time, the diameter of the droplet is continuously shrinking while the contact angle θ_a remains constant (**Figure III-2.a-c**). From the figure, the droplet edge is allowed to move (*i.e.* the edge is unpinned) with a constant contact angle due to the hydrophobic condition of a surface which correlates to low surface energy. On the other hand, a hydrophilic surface with high surface

energy does not allow the droplet edge to move (*i.e.* the droplet edge is pinned). Once the edge is pinned, the evaporation rate of the droplet edge and the center are not constant and the contact angle θ_a decreases over time. This causes a concentration gradient inside the droplet, pulling particles toward the edge and results in a coffee-ring pattern (**Figure III-2.d-f**).

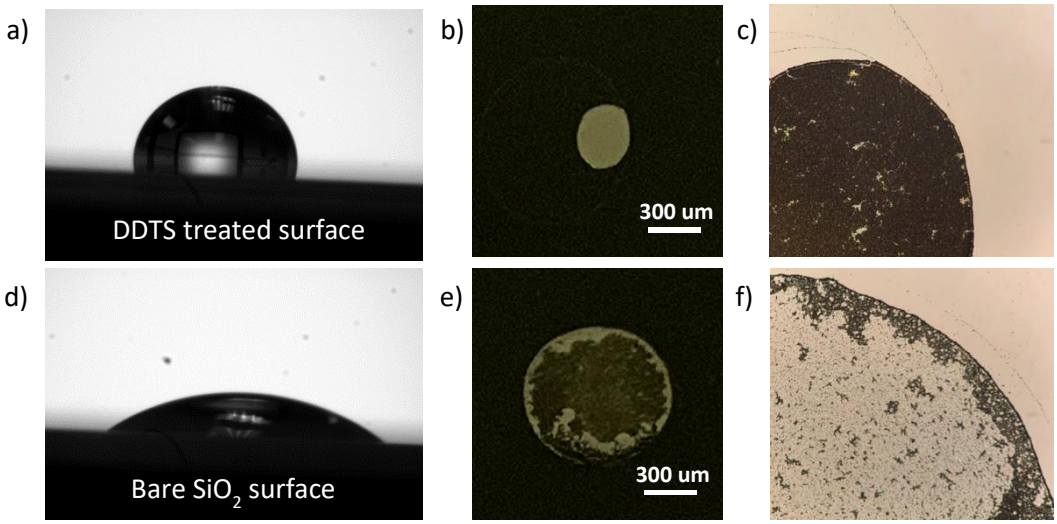

Figure III-3 a) DI water droplets on DDTS-treated SiO_2 surface with the measured contact angle of 103°. b) MoS_2 assembly formed on DDTS-treated surface. c) Magnified optical microscope image of MoS_2 assembly formed on DDTS-treated surface. d) DI water droplets on bare SiO_2 surface with the measured contact angle of 38.9°. b) MoS_2 assembly formed on bare surface. c) Magnified optical microscope image of MoS_2 assembly formed on bare surface.

To achieve a uniform and dense assembly of MoS_2 nanoparticles, we investigated the effect of SAM treatment on the SiO_2 surface experimentally. **Figure III-3** shows a formation of MoS_2 assemblies dependence of SAM treatment. Herein, DDTS is chosen as a SAM material, because its highly hydrophobic functional chain is expected to suppress the coffee-ring effect effectively. The contact angle of a DI water is measured on a bare and a DDTS-treated SiO_2 surfaces. For the given DDTS treatment, the single droplet of DI-water has a higher contact angle (θ_a = 103°) (**Figure III-3.a**) than that of the bare SiO_2 surface (θ_a = 39°) (**Figure III-3.d**). **Figure III-3.e** shows the optical microscope image of an evaporated droplet assembly of MoS_2

nanoparticles formed on bare SiO_2 surface with a coffee-ring pattern. The pattern suggests that the contact edge of the droplet was pinned and an assembly of MoS_2 nanoparticles resulted in a non-uniform ring formation. From the magnified image **Figure III-3.f**, it is clearly seen the MoS_2 particles (dark-colored) are packed along the edge and rest are sparsely distributed inside the dried pattern. On the contrary, **Figure III-3.b** and **Figure III-3.c** shows an optical micrograph of a MoS_2 assembly formed on DDTS-treated surface, the MoS_2 particles are densely packed and distributed uniformly inside a circular pattern. The uniformly distributed pattern implies that the contact angle of the droplet was kept constant during the evaporation and as a result, MoS_2 nanoparticles distributed uniformly without the concentration gradient in the dried pattern.

III.1.2 Printed AgNP electrodes on MoS_2 assembly

A uniform MoS_2 assembly is prepared by drop-casting the MoS_2 suspension on the SAM-treated SiO_2 substrate. As a next step to fabricate **Figure III-1**, electrodes is deposited on MoS_2 assembly, then the printed semiconducting layer. Although Au electrodes fabricated with conventional lithographic methods are stable in ambient and have outstanding electrical characteristics, the lift-off process can damage or remove the MoS_2 assembly. Therefore, this printing method is chosen as an additive process for depositing the bottom-contact architecture on MoS_2 assembly. Herein, silver nanoparticle (AgNP) inks were patterned by inkjet printing as source-drain electrodes.

Figure III-4 shows a SEM image of a densely packed MoS_2 assembly. The particle sizes vary from tens of nano-meter to a few micrometer. These particles are not linked and rather stacked which results in voids inside the assembly. This morphology can be problematic when depositing other materials on top of it because not only the surface is rough but also fluid can flow through an unwanted direction.

Figure III-5 is a SEM image of silver nanoparticles printed on a MoS_2 assembly. Silver was initially designed to print as a straight line (green region) but the magnified image shows that

silver ink flows and wets along MoS_2 particles. The channel length between the designed Ag source and drain is less than 50 μm; however, the wet region exceeds a hundred micron, which means the distance between the source and drain has decreased. The wetting is due to the surface energy difference between the SiO_2 substrate and MoS_2 nanoparticles; the silver has more affinity to MoS_2 than SiO_2. This effect can be fixed by changing the surface energy with a SAM layer. Hence, HMDS was drop-casted on top of the MoS2 assembly to modify the surface energy between SiO_2 and MoS_2. Here, HMDS was chosen as a SAM material because HMDS can simply be drop-casted and evaporates fast. The drop-casted SAM layer is less elaborate than the immersed SAM layer, but still effective in modifying surface energies and favourable for the samples not applicable for immersion method. The surface modification prevents excessive wetting and spreading of silver ink. The device fabricated with a modified surface did not show any short, and well-defined features could be successfully printed.

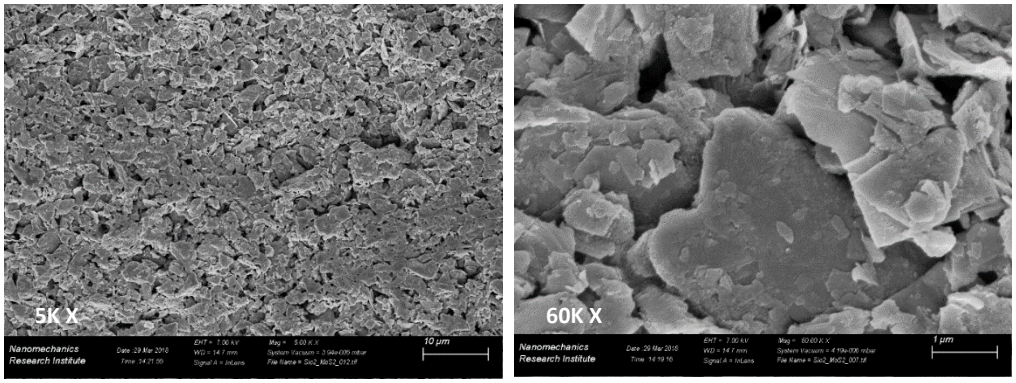

Figure III-4 Scanning electron microscope (SEM) images of a MoS_2 assembly with 5k (left) and 60k (right) magnification.

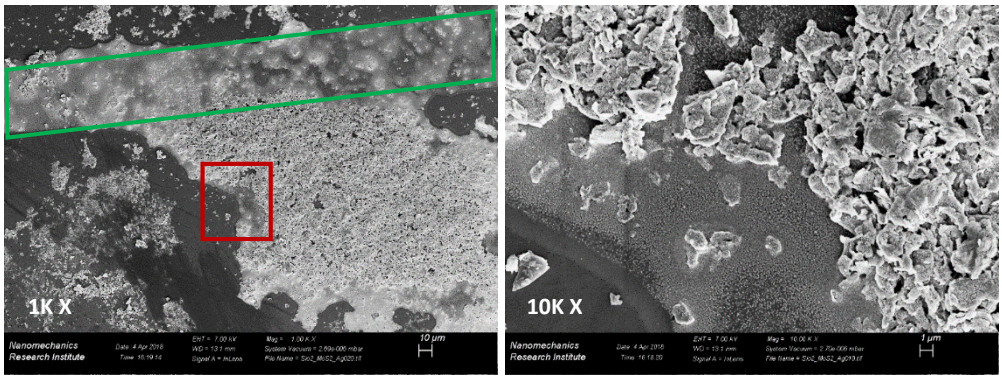

Figure III-5 Scanning electron microscope (SEM) images of AgNP line printed on a MoS_2 assembly with 1k (left) and 10k (right) magnification. The AgNP line was initially printed on the green marked region, then wet along MoS2 particles. 10k magnified image is of red marked region.

III.1.3 Device fabrication process

Highly doped p-type silicon substrates with thermally grown 100 nm thickness silicon dioxide were cleaned by a standard solvent cleaning method. Acetone, isopropanol, and deionized water were used sequentially in an ultrasonic bath. The wafer was then immersed in 0.1 % dodecyltrichlorosilane (DDTS) (Sigma-Aldrich) with toluene mixture for 30 min to form a self-assembled monolayer on the dielectric surface. To avoid the coffee-ring effect, the wetting of the MoS_2 suspension was controlled by modulating the surface energy of the SiO_2 with DDTS.

Dispersed molybdenum disulfide (MoS_2) nanoparticles (Sigma-Aldrich) in DI-water with a concentration of 0.1 mg/ml, and mixed within an ultrasonic bath for 30 min. The prepared MoS_2 suspension was then drop-casted onto the SiO_2 surface. The wafer was place on a hotplate having a temperature of 50 °C for 30 min to evaporate DI-water and form MoS_2 assembly. The temperature was set to slow down the evaporation because fast evaporation at high temperature impedes uniform pattern forming. After drying, hexamethyldisilazane (HMDS) was drop-casted covering the MoS_2 assembly. Silver nanoparticle ink (Advanced Nano Products) was inkjet printed on the MoS_2 assembly to pattern the source and drain contacts. The channel dimensions were defined to be a width of 47 μm and a length of 15 μm. The Ag pattern was then sintered at 200 °C for 30 min under a nitrogen environment. The

organic polymer, poly(3-hexylthiophene) (P3HT) (95.7 % regioregularity, Ossila), was dissolved in 1,2-dichlorobenzene (Sigma-Aldrich) while the solution was heated to 85 °C for 1 hr on a hotplate. The concentration of P3HT solution was 5 mg/ml. The ink formulation was then inkjet-printed onto the channel region on MoS_2 assembly followed by a 130 °C anneal for 30 min in a nitrogen ambient.

The fabricated devices are characterized dc-biased in the current and voltage (I-V) measurement using a Keithley 2400 and Keithely 6430 in air and dark conditions.

III.1.4 Measurement result and characterization

Current-voltage (I-V) measurements were carried out on the fabricated MoS_2-P3HT composite channel TFT under dark conditions at room temperature. The transfer characteristics of the device are shown in **Figure III-6** and key parameters are summarized in **Table III-1**. The device was measured in saturation mode (V_{DS} = - 60 V) and linear mode (V_{DS} = - 10 V) at different drain voltages (V_D).

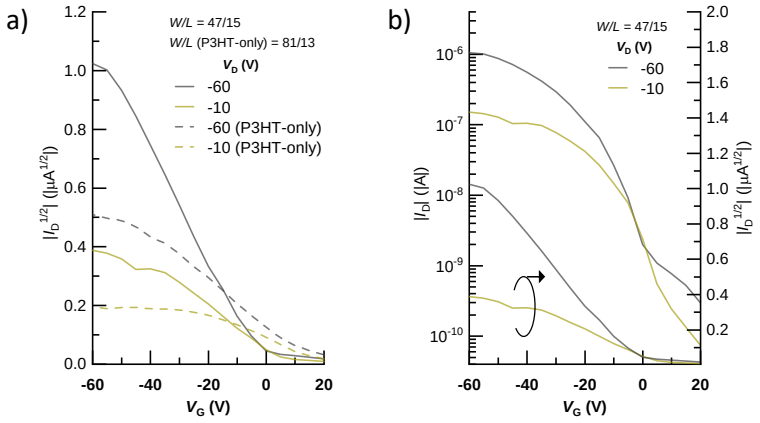

Figure III-6 a) Transfer characteristics of P3HT-only TFTs and MoS_2-P3HT hybrid TFTs with drain voltage (V_D) of −10 V and −60 V in square root. b) Transfer characteristics of MoS_2-P3HT hybrid TFTs with drain voltage (V_D) of −10 V and −60 V in logarithmic scale (left axis) and square root (right axis).

Table III-1 Device parameters of P3HT-only TFTs and MoS_2-P3HT hybrid TFTs.

	$\mu_{sat.}$ (cm^2/V-s)	V_{TH} (V)	*S.S* (V/dec.)
Hybrid	8.00×10^{-3}	-3.96	-12.08
P3HT-only	8.00×10^{-4}	24.97	-20.89

In **Figure III-6.b**, based on the plot of square root of I_D, the threshold voltage (V_{TH}) was extracted to a value of – 3.96 V. While OTFT devices usually have inherent charge trap states at the interface between the polymer and the dielectric with defect states in the organic film itself [90], the I-V characteristics of the measured hybrid devices were relatively stable compared to other reported hybrid channel devices using carbon-based 2-D materials [67], [74]. A high contact resistance from the Ag electrode is observed as a slight roll-off in the drain current when the applied gate voltage (V_G) is near − 60 V, while in the device is in saturation mode. We expect that the degraded saturation current at high gate voltage may be due to a work function difference between the semiconductor and metal contact resulting in a Schottky barrier. The highly occupied molecular orbital (HOMO) level of P3HT is reported near – 5.1 eV. On the contrary, the fermi level of Ag lies at – 4.3 eV. This difference in energy level creates a barrier to the hole-charge injection and degrades device performance. However, this problem can be addressed by SAM treatment tune the work function of Ag electrodes [91], and further investigations are underway.

Considering the I_D in a logarithmic scale, the MoS_2-P3HT composite TFT displays the switching characteristics of a transistor. The on/off ratio was observed to be more than three orders of magnitude in both saturation and linear mode. The saturation field-effect mobility was calculated by the gradual-channel approximation. Based on the I-V measurement result, the calculated mobility is 8.0×10^{-3} cm^2/V-s. The field-effect mobility of the hybrid TFT is higher compared to the only-P3HT device ($\mu_{sat.} = 8.0 \times 10^{-4}$ cm^2/V-s) fabricated with the same condition. The normalized on-current with respect to W/L also increased by an order of magnitude when MoS_2 nanoparticles are introduced to the channel region **Figure III-6.a**. Compared to previous studies of printed Ag electrode with spin-coated P3HT TFTs [92] or printed P3HT on patterned gold source-drain TFTs [86], both the P3HT-only and hybrid devices have

comparable electrical characteristics. This result shows printed materials (*i.e.* metal nanoparticle and organic polymer) can potentially work well within a TFT device structure and provides a novel approach for all printed OTFTs.

III.2 MoS_2-P3HT hybrid ink formulation

From III.1.4, we observed an assembly of MoS_2 nanoparticles enhanced electrical characteristics of P3HT TFTs by incorporating with the semiconducting polymer film. Meanwhile, a liquid exfoliation method is designed to simply the integration process of nanomaterials, which allows the formation of hybrid and composite materials [64], [65]. Combining these benefits to the MoS_2-P3HT composite channel, we exfoliated nanoparticles in a semiconducting polymer solution, and prepared it as a MoS_2-P3HT hybrid ink. It simplifies processing by eliminating pre- and post-processing steps required for forming a MoS_2 assembly, plus gives more freedom in defining electrodes for TFT devices. Moreover, the hybrid ink expands the usage of nanoparticles into printing and large-area applications.

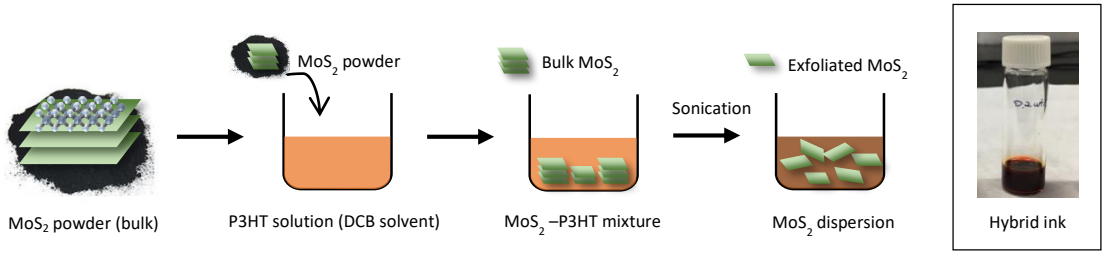

Figure III-7 An illustration of MoS_2-P3HT hybrid ink formulation procedure. MoS_2 powder is blended into P3HT solution and sonicated. During the sonication, interlayers of MoS_2 exfoliated into single or a few layers of MoS_2 and dispersed in a solvent. The picture of formulated hybrid ink (0.2 wt%) is shown.

Figure III-7 shows our suggested MoS_2-P3HT hybrid solution (MoS_2 suspended in a P3HT solution) preparation steps. The organic polymer, P3HT (95.7 % regioregularity, Ossila), is dissolved in 1,2-dichlorobenzene (Sigma-Aldrich) while the solution was heated to 85 °C for 1 hr on a hotplate. The MoS_2 nanoparticles (90 nm diameter, Sigma-Aldrich) are then weighed and blended into the solution with the desired concentrations (*i.e.* 0.2 wt%). The powdered MoS_2 is mostly bulk and layered, coupled via weak van der Waals force between interlayers. The layers can be separated by exfoliation. The blended solution is sonicated for 30 min to

make MoS_2 particles exfoliated and well dispersed in an organic solvent. The finally prepared hybrid ink with concentration of 0.2 wt% in 10 mg/ml P3HT solution is shown in the figure.

It should be noted that if the hybrid ink is left stagnant for more than 10 min, the MoS_2 particles will start to aggregate and sink down to the bottom of the liquid carrier; due to this observation, the ink is typically processed immediately after the sonication step. Due to the limited lab equipment, the proposed process is not ideal for nanoparticle exfoliation and the final solution may contain nanoparticle bulk material which are not completely exfoliated. The future work includes exfoliation of MoS_2 with advanced liquid exfoliation technique, such as centrifugation, high-sheer mixing, and microfludization [64], [93].

III.3 Spin-coated MoS_2-P3HT hybrid TFT

III.3.1 Spin-coated hybrid ink device fabrication process

A spin-coated MoS_2-P3HT hybrid channel TFT is designed as **Figure III-8** and fabricated to investigate the electrical performance of MoS_2-P3HT hybrid film.

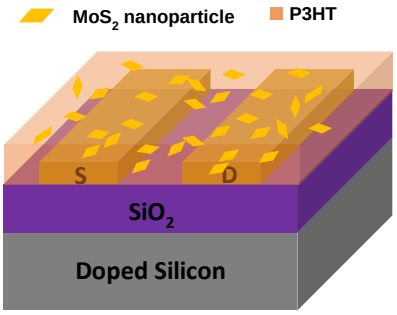

Figure III-8 Schematic device structure of a spin-coated MoS_2-P3HT hybrid TFT with a bottom-gate, bottom-contacts structure.

MoS_2-P3HT hybrid ink (MoS_2 suspended in a P3HT solution) was prepared as described in III.2. 0.8 wt% concentrations of MoS2 nanoparticles are blended into 10 mg/ml P3HT solution. During the ink preparation, exposure to air and UV light was avoided. The whole process was the same as general fabrication process of spin-coated P3HT TFTs as described in I.3 and II.1.2.

Highly doped p-type silicon substrates were used as the common bottom gate structure with thermally grown 100 nm thickness silicon dioxide as a dielectric layer. The source and drain electrodes were patterned by conventional photolithography and 2 nm Cr as an attachment layer and 40 nm Au as a charge injection layer was thermally deposited. The channel dimension of the device was 1000 μm in width and 30 μm in length.

Prepared patterned substrates were cleaned with Isopropyl alcohol, acetone, and deionized water sequentially then treated with oxygen plasma to remove possible remaining organics. HMDS was used as a SAM material to improve the molecular ordering of the polymer thin film formation and to control the wettability of SiO_2 and Au by modifying surface energies.

The MoS_2-P3HT composite film was spin-coated on the HMDS-treated surface at 3000 rpm for 80 s (using an acceleration of 800 rpm/s) under nitrogen condition. The middle part of the hybrid ink in the vial was taken for spin-coating use for yielding MoS_2 suspension without aggregations or sinks. The devices were then oven-annealed in a vacuum for 1 hr at the ramped up temperature from room temperature to 120 °C. Finally, the fabricated devices were characterized as pulsed in the current and voltage (I-V) measurement using a Keithley 2400 under vacuum and dark conditions.

III.3.2 Measurement result and characterization

Current-voltage (I-V) measurements were carried out on the spin-coated MoS_2-P3HT hybrid TFT under vacuum and dark conditions at room temperature.

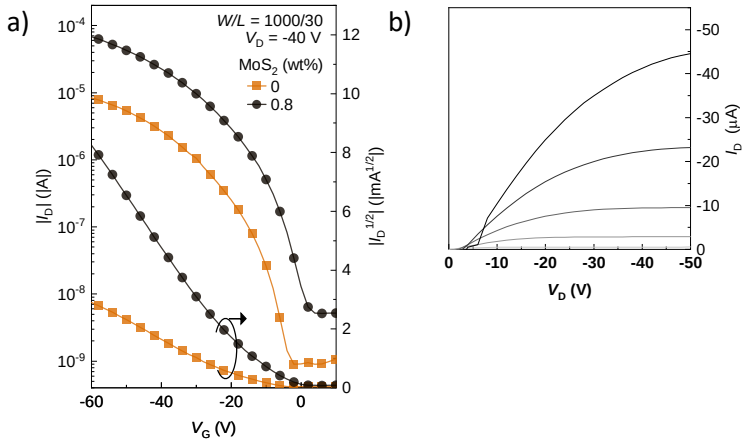

Figure III-9 a) Transfer characteristics of P3HT-only TFTs and MoS_2-P3HT hybrid TFTs (0.8 wt%) in logarithmic scale (left axis) and square root (right axis). b) I_D-V_D of MoS_2-P3HT hybrid TFTs (V_G = -10, -20, -30, and -40 V).

Table III-2 Device parameters of P3HT-only TFTs and MoS_2-P3HT hybrid TFTs (0.8 wt%).

	$\mu_{sat.}$ [a)] (cm^2/V-s)	V_{TH} [a)] (V)	$S.S$ [a)] (V/dec.)	I_{ON}/I_{OFF} [a)]
P3HT-only	$(9.81 \pm 5.27) \times 10^{-3}$	-14.44 ± 1.83	-5.69 ± 0.43	$(6.48 \pm 4.37) \times 10^{3}$
0.8 wt% MoS_2	$(5.12 \pm 0.33) \times 10^{-2}$	-12.17 ± 1.23	-8.81 ± 2.01	$(1.05 \pm 0.40) \times 10^{4}$

a) average of 9 devices

Figure III-9.a compares transfer characteristics of a P3HT-only TFT and a 0.8 wt% hybrid TFT at a constant drain voltage (V_D) of −40 V, in saturation regime. It is observed that the on-current increases when MoS_2 nanoparticles are blended into P3HT; the on-current of the 0.8 wt% MoS_2 blended device was almost one order of magnitude higher than the baseline device (*i.e.* P3HT-only TFT).

The hole field-effect mobility in the saturation regime was calculated by the gradual-channel approximation. The threshold voltage, V_T, was determined using a linear fit to the square root of drain current versus gate voltage. These calculated values are summarized in **Table III-2**. The field-effect mobility increased with the existence of MoS_2. The field-effect mobility of MoS_2-P3HT hybrid TFT (0.8 wt% MoS_2) is 5.12×10^{-2} cm^2/V-s which is higher than the baseline device, 9.81×10^{-3} cm^2/V-s. This measurement result shows that the fabricated TFT has a relatively smaller shift of a threshold voltage of -12.17 V, and better the on/off ratio of 1.34×10^{-4} compare with previous studies of organic-inorganic hybrid TFTs summarized in I.6.2.

The output characteristics of hybrid TFT is shown in **Figure III-9.b**. The drain current was measured as a function of drain voltage (V_D) with different gate bias voltages (V_G) under dark conditions. The range of drain bias voltages is swept from 0 V to -50 V in a step of -2 V. The output curve depicts the modulated drain current by an applied drain voltage. The output characteristics showed good saturation behaviour with clear saturation currents. However, in the linear regime, the device did not turn on immediately at VD ~ 0 V, a minor shift was observed. We assume there is an energy barrier at the electrode-semiconductor interface which requires higher drain voltage to initiate the current to flow through the channel. The

quality of source-drain electrodes or the film quality at the electrode-semiconductor interface are possible factors. At the electrode-semiconductor interface, the work function of Au and the HOMO level of P3HT matches. However, the adhesion layer Cr and P3HT display the Schottky barrier height of 0.3 eV, which may work as a charge injection barrier. This will be more investigated under future work. In the saturation regime, it was observed that nanocomposite TFT has a higher on-state current than P3HT-only TFT. These results provide experimental evidence of the MoS_2 enhancing the charge transport characteristic of the organic TFT device performance.

III.3.3 TFT device performance for varying MoS_2 concentrations

An additional experiment is designed to identify if the concentration of MoS_2 nanoparticles is correlated to the improvement of electrical characteristics. Various MoS_2 concentrations of 0.05, 0.2, 0.5, and 0.7 wt% are selected to fabricate MoS_2-P3HT hybrid TFTs. The device fabrication processes and characterizations followed the same procedure with previously fabricated 0.8 wt% hybrid TFTs in III.3.1.

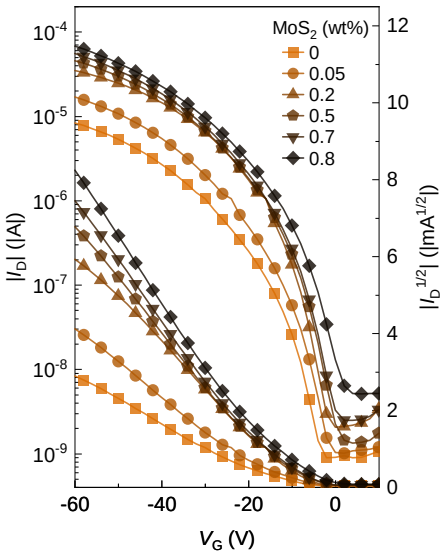

Figure III-10 Transfer characteristics of MoS_2-P3HT hybrid TFTs with various concentrations of MoS_2 (0, 0.05, 0.2, 0.5, 0.7, and 0.8 wt%) in logarithmic scale (left axis) and square root (right axis).

Table III-3 Device parameters of MoS_2-P3HT hybrid with various concentrations of MoS_2 (0, 0.05, 0.2, 0.5, 0.7, and 0.8 wt%).

MoS2 (wt%)	$\mu_{sat.}$ [a)] (cm^2/V-s)	V_{TH} [a)] (V)	$S.S$ [a)] (V/dec.)	I_{ON}/I_{OFF} [a)]
0	$(9.81 \pm 5.27) \times 10^{-3}$	-14.44 ± 1.83	-5.69 ± 0.43	$(1.16 \pm 0.56) \times 10^4$
0.05	$(1.80 \pm 0.41) \times 10^{-2}$	-14.07 ± 0.89	-6.71 ± 0.45	$(1.44 \pm 0.67) \times 10^4$
0.2	$(3.12 \pm 0.22) \times 10^{-2}$	-9.27 ± 1.14	-6.6 ± 1.72	$(1.48 \pm 1.17) \times 10^4$
0.5	$(3.46 \pm 0.16) \times 10^{-2}$	-11.77 ± 0.90	-10.56 ± 4.51	$(1.48 \pm 1.64) \times 10^4$
0.7	$(4.86 \pm 0.34) \times 10^{-2}$	-12.02 ± 0.50	-8.56 ± 2.64	$(1.15 \pm 0.82) \times 10^4$
0.8	$(5.12 \pm 0.33) \times 10^{-2}$	-12.17 ± 1.23	-8.81 ± 2.01	$(9.78 \pm 6.40) \times 10^3$

a) average of 9 devices

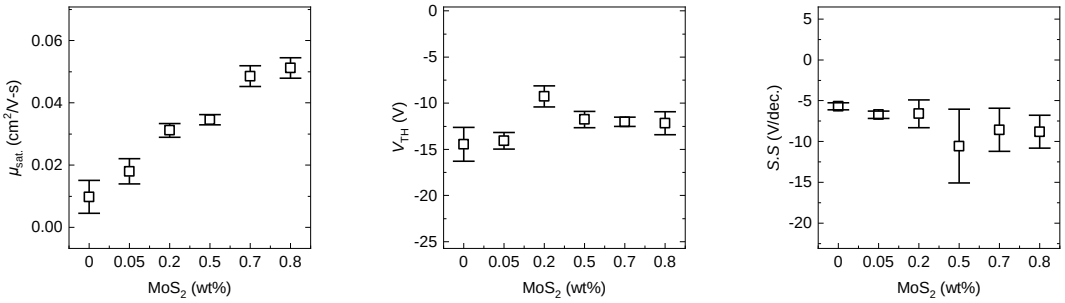

Figure III-11 Device parameters distributions of MoS_2-P3HT hybrid with various concentrations of MoS_2 (0, 0.05, 0.2, 0.5, 0.7, and 0.8 wt%).

Figure III-10 shows a transfer curve of hybrid TFTs with 6 different MoS_2 concentrations: 0, 0.05, 0.2, 0.5, 0.7, and 0.8 wt%. The devices have a width of 1000 μm and a length of 30 μm and I_D-V_G is measured at V_D = -40 V which is in a saturation region. It is observed that as the concentration of MoS_2 increases, the on-current increases as well. The off-current tends to increase too, but with smaller differences compare to the on-current increment. **Table III-3** summarizes the figure of merits: field-effect mobility, threshold voltage, subthreshold swing, and on/off ratio. All the values are an average of 9 devices with their deviations. The field-effect mobility continuously increases with increasing concentration of MoS_2. This trend can be also seen in **Figure III-11**. The increment of field-effect mobility is not proportional to the concentration of MoS_2 but the addition of a small amount of MoS_2 (0.05 wt%) made a distinct

change in both on-current and mobility. In other words, the existence of MoS_2 in a polymer film apparently improves the electrical characteristics. Moreover, the alignment of the HOMO level of P3HT and the conduction band maximum of MoS_2 attributed to the high hole charge transport. The energy barriers between materials may hinder the overall conductivity in the film. The threshold voltage difference between different concentrations was 5 V at most (maximum of -14.44 V from 0 wt% and minimum of -9.27 V from 0.2 wt%). The threshold voltage and subthreshold swing did not show trends but within a similar range overall as shown in **Figure III-11**.

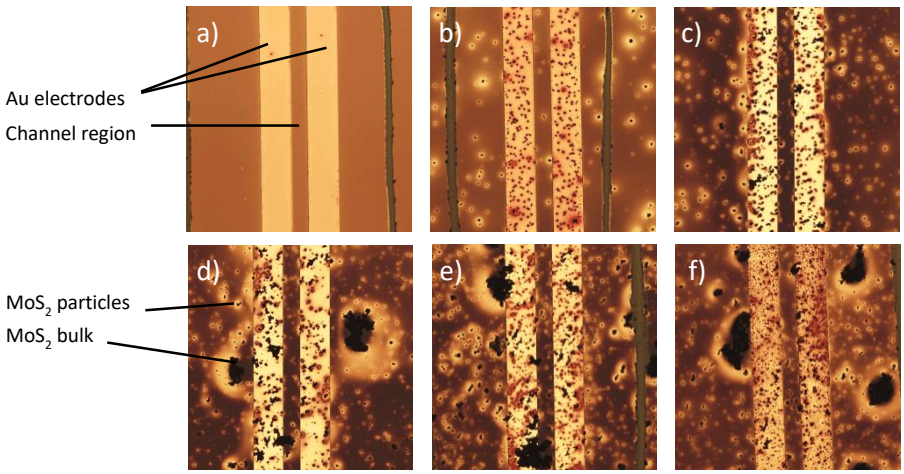

Figure III-12 Optical microscope image of MoS_2-P3HT hybrid with various concentrations of MoS_2: 0, 0.05, 0.2, 0.5, 0.7, and 0.8 wt% ((a)-(f)). The bright region is Au electrodes; the polymer is coated over the SiO_2 substrate and electrodes; dark parts are MoS_2 particles and bulks. L = 30 um.

On/off ratio of various concentrations are also showing no big difference except 0.8 wt% sample which is lower than other concentrations. This is due to the high off-current on average which is correlated to bulk MoS_2 in the channel region. Moreover, the large deviations of the on/off ratio can be correlated to the existence of the bulk MoS_2 too. Nine devices with the same MoS_2 concentration were all fabricated on a single substrate and spin-coated with the hybrid ink simultaneously. The random distribution of MoS_2 bulks in the spin-coated film affected off-currents of each device, and resulted in large deviations. **Figure III-12** shows an

optical microscope image of spin-coated hybrid TFTs with various MoS_2 concentrations. **Figure III-12.a** is a pristine P3HT film coated on Au source-drain patterned SiO_2. MoS_2 particles start to be seen once MoS_2 is blended into the film. As the MoS_2 concentration increases, the number of particles increases as well but also the larger "bulk" MoS_2 clusters start to become visible. This may be because the MoS_2 concentration exceeded the percolation threshold. Above this percolation threshold, the mobility and on-current keep increases, but limited due to the crystallinity of polymer. However, the off current increases significantly due to the formed percolation paths, which is not desirable for the switching characteristics of the transistors [12], [67], [66].

Since the existence of bulk MoS_2 in the channel region is troublesome, we tried to remove it. The hybrid ink was filtered with a 5 μm PTFE filter to remove the aggregated MoS_2 particles. The electrical characteristics are compared with a device fabricated with a non-filtered hybrid solution, with the key parameters extracted from measured data are summarized in

Table *III-4*. The field-effect mobility decreased but not significantly after filtering the ink; apparently, the final concentration of the hybrid ink reduced due to the removal of some MoS_2 particles. However, the on/off ratio increased significantly, even higher than other devices fabricated with various concentrations (**Table III-3**). The enhancement in on/off ratio is attributed to the removal of bulk MoS_2 in the channel region that keeps off-current low, and increased on-current due to MoS_2 nanoparticles in the film. The change in particle sizes and the density can be observed in an optical microscope image in **Figure III-13**. Micron-size bulks are removed after filtering and also the number of visible particles are reduced.

Table III-4 Device parameters of MoS_2-P3HT hybrid TFT (0.8 wt%) fabricated with unfiltered and filtered hybrid inks. 5 μm pore size PTFE filter was used.

MoS2 (wt%)	$\mu_{sat.}$ [a)] (cm^2/V-s)	V_{TH} [a)] (V)	$S.S$ [a)] (V/dec.)	I_{ON}/I_{OFF} [a)]
0.8 (unfiltered)	$(4.59 \pm 0.24) \times 10^{-2}$	-7.43 ± 1.67	-11.54 ± 3.98	$(7.17 \pm 5.60) \times 10^{3}$
0.8 (filtered)	$(3.23 \pm 0.45) \times 10^{-2}$	-7.90 ± 1.13	-12.31 ± 1.51	$(2.52 \pm 1.88) \times 10^{4}$

a) average of 6-9 devices

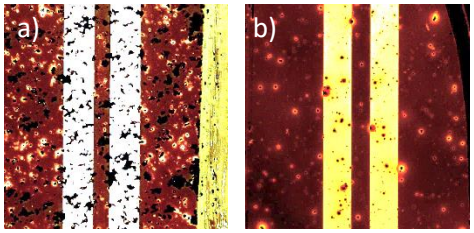

Figure III-13 Optical microscope image of a MoS_2-P3HT hybrid TFT (0.8 wt%) fabricated with a) unfiltered and b) filtered hybrid inks. 5 μm pore size PTFE filter was used. L = 30 um.

The enhancement in electrical characteristics is observed in hybrid TFTs incorporating P3HT and MoS_2, as an organic semiconductor and inorganic material, respectively. Organic semiconductors follow a hopping transport mechanism due to the high density of impurities and traps. The charge transport is by hopping between localized sites and this limits the conductivity of organic materials [20]. On the other hand, in bulk crystal-like MoS_2, the charge transport is along the conduction band [94]. In a view of molecular ordering, increased mobility with a higher concentration of MoS_2 is due to increased crystallinity of P3HT with the presence of MoS_2 particles. Some studies showed an improvement in the crystallinity of polymer film through AFM, X-ray diffraction, and UV-visible measurements [76], [95], [72], [75]. Moreover, the higher concentration of MoS_2 provides an effective pathway for charge carriers in the composite film [12], [67]. The hole mobility in monolayer sheets of MoS_2 reported from the previous study was 96.62 cm^2/V-s [96]. Hence, we speculate that MoS_2 works as a conducting path within the organic film due to its high mobility. However, one study shows that the mobility of individual flakes of liquid-exfoliated MoS_2 is lower than mechanically exfoliated MoS_2 flakes [64]. This can be a bottleneck of improving the electrical characteristics of hybrid TFTs to reach higher mobility.

III.4 Printed MoS_2-P3HT hybrid TFT

III.4.1 Fabrication issue of printed MoS_2-P3HT hybrid TFT

Printing nanoparticles may convey some problems. The problems are mostly owing to the compatibility between nanoparticle sizes and nozzle sizes. Even though each nanoparticle is nano-size, due to van der Waals force between interlayers, particles can stack into multi layers and possibly form a micron-size bulk. This bulk causes a nozzle clogging issue in an inkjet printing system. Different dispensers have different nozzle dimensions. For example, a multi-ejector cartridge printhead is designed to jet droplets having a volume of 10 pl. When converting the volume into a cubic meter, the generated drop diameter is around 10 μm. This means when a bulk of particles larger than 10 μm is suspended in the ink for jetting, the particles may block the nozzle. The use of a single nozzle ejector with a variety of nozzle diameters from 20 μm to 80 μm is more compatible with micron-size particles. Still, there is a possibility bulks to block the nozzle or to disturb jetting by floating near the nozzle tip.

To eliminate this problem, nanoparticle inks should be filtered before loading into the printer. Here, a hydrophobic PTFE syringe filter with a pore size of 5 μm (Membrane Solutions) is used to remove aggregated nanoparticles of micron-size. This filter is previously used from III.3.3 to remove bulk MoS_2 in the spin-coated hybrid film. However, the filtered solution is only compatible with the Microfab nozzle used in the Ceradrop printing system. A few micron size particles remaining in the solution are big enough to clog multi nozzle heads ($d < 10$ μm). There are smaller pore-sized filters down to 0.1 μm but it encounters another issue. When filtering the ink, flakes larger than the pore size stack onto the membrane and finally all the pores are blocked so that no liquid can flow through the filter. This phenomenon is observed with 1 μm pore-size filter.

Herein, it is demonstrated that filtered nanoparticle suspended solutions using a 5 μm pore-size filter and printing the filtered ink using an 80 μm Microfab nozzle removed many of the clogging issues.

III.4.2 Device fabrication process

Figure III-14 shows a schematic device structure of a printed MoS_2-P3HT hybrid channel TFT having a coplanar bottom-gate structure.

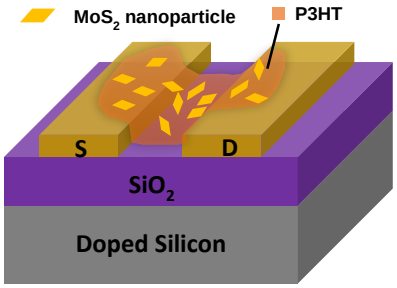

Figure III-14 Schematic device structure of a printed MoS_2-P3HT hybrid TFT with a bottom-gate, bottom-contacts structure.

MoS_2-P3HT hybrid ink (MoS_2 suspended in a P3HT solution) was prepared as described in III.2 with 0.8 wt% concentrations of MoS_2 nanoparticles blended into 5 mg/ml P3HT solution; the P3HT concentration is selected based on the discussion in II.2.1 (**Table II-6**). During the ink preparation, exposure to air and UV light is avoided. The pristine P3HT solution is also prepared to compare as a baseline.

Highly doped p-type silicon substrates were used as the common bottom gate structure with thermally grown 100 nm thickness silicon dioxide as a dielectric layer. The source and drain electrodes were patterned by conventional photolithography and 2 nm Cr as an attachment layer and 40 nm Au as a charge injection layer was thermally deposited. The channel dimension of the device was 1000 μm in width and 30 μm in length.

Prepared patterned substrates were cleaned with Isopropyl alcohol, acetone, and deionized water sequentially then treated with oxygen plasma to remove possible remaining organics. HMDS was used as a SAM material to improve the molecular ordering of the polymer thin film formation and to control the wettability of SiO_2 and Au by modifying surface energies.

The hybrid ink was filtered with a hydrophobic PTFE syringe filter with a pore size of 5 μm (Membrane Solutions) to remove bulk MoS_2. Then the filtered ink is loaded and ejected using Microfab single nozzle with 80 μm nozzle diameter. The drop volume was ~90 pl and the drop diameter of printed P3HT on the HMDS-treated SiO_2 substrate was ~110 μm (**Figure III-15**). The drop volume of P3HT-only ink was similar and the diameter was a little larger, ~140 μm. The patterns were printed with 80 μm spacing with 300 Hz jetting frequency. A single line of 1200 μm width and 130 μm length was printed as an active layer on 9 devices consecutively.

The devices were then oven-annealed in a vacuum for 1 hr at the ramped up temperature from room temperature to 120 °C. Finally, the fabricated devices were characterized as pulsed in the current and voltage (I-V) measurement using a Keithley 2400 under vacuum and dark conditions.

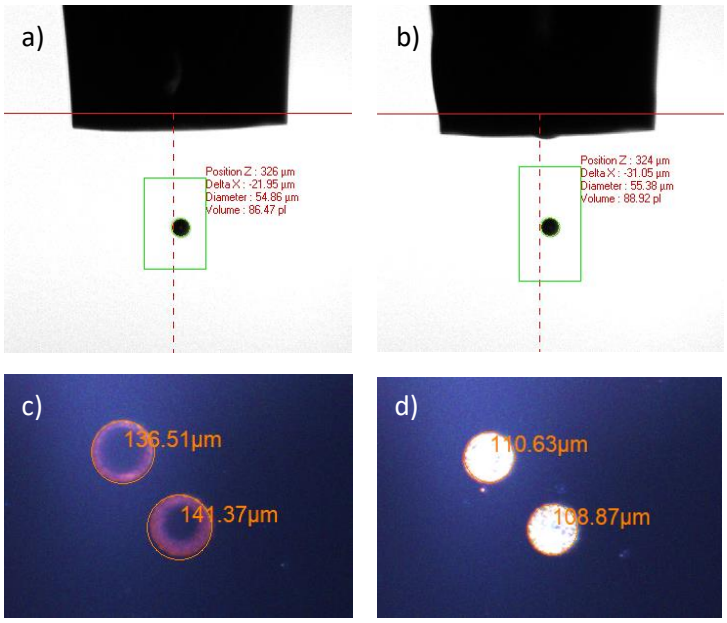

Figure III-15 a) Droplet analysis of P3HT solution. The drop diameter of 54.86 µm and the drop volume of 86.47 pl. b) Droplet analysis of MoS_2-P3HT hybrid ink (0.8 wt%, filtered). The drop diameter of 55.38 µm and the drop volume of 88.92 pl. c) Printed single droplet of P3HT solution with the diameter ~ 140 µm. D) Printed single droplet of MoS_2-P3HT hybrid ink (0.8 wt%, filtered) with the diameter ~ 110 µm.

III.4.3 Measurement result, characterization and analysis

Current-voltage (I-V) measurements were carried out on the printed MoS_2-P3HT hybrid TFT under vacuum and dark conditions at room temperature.

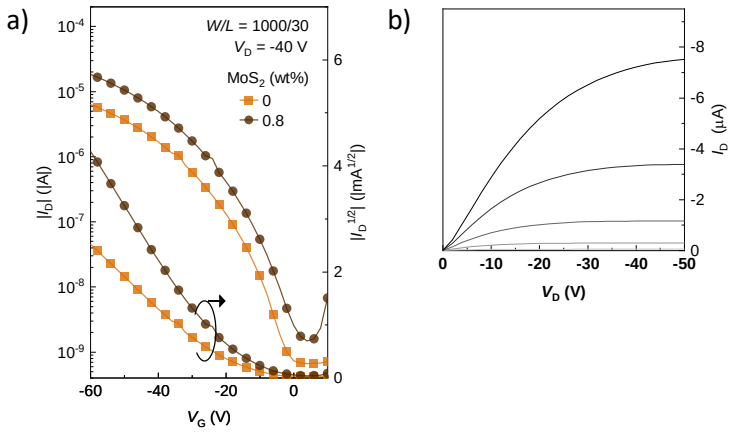

Figure III-16 a) Transfer characteristics of P3HT-only TFTs and MoS_2-P3HT hybrid TFTs (0.8 wt%, filtered) fabricated via printing in logarithmic scale (left axis) and square root (right axis). b) I_D-V_D of MoS_2-P3HT hybrid TFTs (V_G = -10, -20, -30, and -40 V).

Table III-5 Device parameters of P3HT-only TFTs and MoS_2-P3HT hybrid TFTs (0.8 wt%, filtered) fabricated via printing and spin-coating.

	MoS2 (wt%)	μ_{max} (cm^2/V-s)	$\mu_{sat.}$ [a] (cm^2/V-s)	V_{TH} [a] (V)	$S.S$ [a] (V/dec.)	I_{ON}/I_{OFF} [a]
Printing	0	1.05×10^{-2}	$(7.07 \pm 1.71) \times 10^{-3}$	-17.19 ± 1.15	-9.32 ± 2.24	$(9.62 \pm 3.83) \times 10^{3}$
	0.8	2.35×10^{-2}	$(1.85 \pm 0.32) \times 10^{-2}$	-17.87 ± 1.39	-8.60 ± 0.92	$(1.23 \pm 0.48) \times 10^{4}$
Spin-coating	0.8	4.13×10^{-2}	$(3.23 \pm 0.45) \times 10^{-2}$	-7.90 ± 1.13	-12.31 ± 1.51	$(2.52 \pm 1.88) \times 10^{4}$

a) average of 6-9 devices

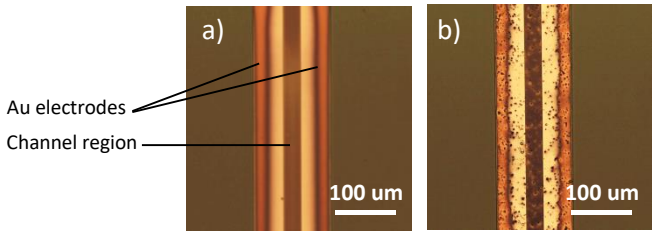

Figure III-17 Optical microscope image of a) a printed P3HT TFT and b) a MoS_2-P3HT hybrid TFT (0.8wt%, filtered). The bright region is Au electrodes; the polymer is coated over channel region and electrodes; dark particles are MoS_2. L = 30 um.

Figure III-16.a compares transfer characteristics of a P3HT-only TFT and a 0.8 wt% hybrid TFT at a constant drain voltage (V_D) of −40 V, in saturation regime. It is observed that the on-current increases when MoS_2 nanoparticles are blended into P3HT; the on-current of the 0.8 wt% MoS_2 blended device was half order magnitude higher than the baseline device (*i.e.* P3HT-only TFT).

The hole field-effect mobility in the saturation regime was calculated by the gradual-channel approximation. The threshold voltage, V_T, was determined using a linear fit to the square root of drain current versus gate voltage. These calculated values are summarized in **Table III-5**. The field-effect mobility increased with the existence of MoS_2. The field-effect mobility of MoS_2-P3HT hybrid TFT (0.8 wt% MoS_2) is 1.85×10^{-2} cm^2/V-s which is higher than the baseline device, 7.07×10^{-3} cm^2/V-s. The threshold voltage is within a similar range and the on/off ratio of hybrid TFT was larger than pristine TFT. Also, the deviation of an on/off ratio is observed less in hybrid TFTs, which indicates that the nanoparticles are distributed evenly without aggregations. The distribution of MoS_2 nanoparticles is shown in **Figure III-17.b**.

MoS_2 particles, with no big difference in sizes, are distributed uniformly in the channel region which attributes to little deviations in device performance.

The output characteristics of hybrid TFT is shown in **Figure III-16.b**. The drain current was measured as a function of drain voltage (V_D) with different gate bias voltages (V_G) under dark conditions. The range of drain bias voltages is swept from 0 V to -50 V in a step of -2 V. The output curve depicts the modulated drain current by an applied drain voltage. The output characteristics showed good saturation behaviour with clear saturation currents. In the linear regime, the drain current depicts a linear I-V characteristic indicating these devices are unaffected by the source-drain contact resistance. These results provide experimental evidence of the MoS_2 enhancing the charge transport characteristic of the organic TFT device performance.

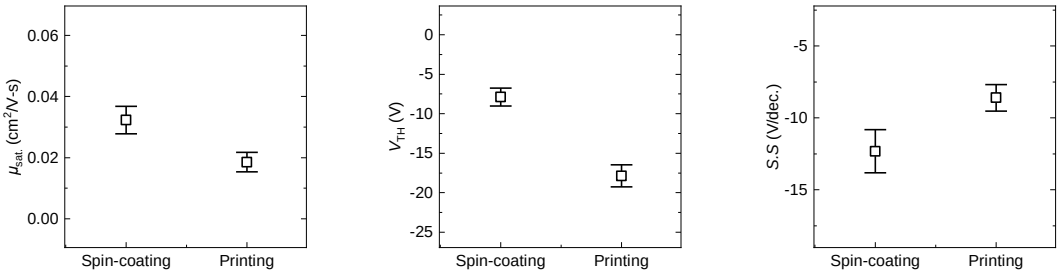

Figure III-18 Device parameters distributions of MoS_2-P3HT hybrid TFTs (0.8 wt%, filtered) fabricated via printing and spin-coating.

From **Table III-5**, the printed devices show a higher threshold voltage compared to the spin-coated devices. However, we speculate this is due to fabrication environment rather than the difference in deposition method between spin-coating and printing; because previously, printed TFTs (II.2.3) shows lower threshold voltage than spin-coated TFTs. The causes of high threshold voltage will be investigated under future work. **Figure III-18** compares field-effect mobility, threshold voltage, and subthreshold swing of spin-coated and printed hybrid TFTs. Spin-coated device shows slightly better electrical performance overall but the results are not

significantly different. Compare with previously reported MoS_2-P3HT hybrid TFT [76], both spin-coated and printed devices show comparable characteristics. Moreover, it is the first time MoS_2-P3HT composite ink was printed and fabricated into devices.

Part IV Conclusions and future work

IV.1 Conclusion

Thin-film transistors containing both semiconducting polymers and inorganic materials were successfully fabricated using a printing method. P3HT and MoS_2 were chosen as a semiconducting polymer and an inorganic material, respectively. The results have shown that field-effect mobilities of MoS_2-P3HT hybrid TFTs were higher than that of P3HT-only baseline TFTs. When fabricating TFTs with MoS_2 suspended P3HT solution (*i.e.* hybrid ink) with concentrations of 0.8 wt%, the field-effect mobility as high as 2.35×10^{-2} $cm^2/V\text{-}s$ can be obtained. This value is more than double the mobility of baseline TFT with an even higher on/off ratio. Filtering the solution keeps MoS_2 from reaching the percolation threshold and prevents the high off-current which is attributed to the existence of MoS_2 bulks in the channel region. At the same time, MoS_2 nanoparticles incorporated into polymer films increase the on-current. Adding MoS_2 nanoparticles into organic semiconductors is suspected to enhance the film crystallinity; moreover, MoS_2 is believed to work as a high transporting region for hole carriers. Meanwhile, mobility and on-current increased with the increasing concentration of MoS_2 in P3HT solutions. However, the relation was not proportional. The percolated bulk MoS_2 may interfere with the homogeneity in the film; hence, hinder the molecular ordering of the P3HT.

To realize printed MoS_2-P3HT hybrid TFTs, OTFT processing and printing parameters were precisely controlled and optimized beforehand. Especially, SAM treatment is important in many aspects. The hydrophobic nature of SAM functional groups enhances polymer chain orientation into a well-defined lamellar structure. It gave high crystallinity to the polymer film which results in twenty times higher field-effect mobility compare to devices fabricated without SAM treatment. SAM also controls a wettability of the treated surface, enabling uniform wetting of polymers on both electrodes and dielectric surfaces. If the surface energy

is not controlled, printed fluid could flow from low to high surface energy, and end up with poor film quality. When printing, parameter settings of back pressure and pulse train are important to achieve stable jetting dynamics. Once jetting parameters are set in a range, the spacing between adjacent droplets should be controlled to attain well-defined patterns. Herein, the printing technique is combined with the MoS_2-P3HT hybrid ink prepared for printing use, an array of MoS_2-P3HT hybrid channel is printed simultaneously on a Au electrodes array without any offset or misprint.

The results imply that the electrical properties of P3HT film were improved by introducing MoS_2 nanoparticles into a film. It is promising that inorganic-organic composite materials can be solution-processed and applied in printing technology since it can be linked to large-area applications beyond transistors in the future.

IV.2 Future work

1. Investigating P3HT film ordering using film characterization tools

The MoS_2-P3HT hybrid TFTs showed better electrical characteristics compared to baseline TFTs. Theoretically, the improved electrical performance is attributed to the enhanced film ordering. However, the assumption needs to be proven experimentally. The effect on the crystalline microstructure including crystallinity and molecular orientation can be investigated with characterization tools. The polymer film characterization is commonly conveyed with an atomic force microscopy (AFM), UV-vis absorption spectroscopy, and X-ray diffraction: AFM shows the size of polymer chains and their ordering; UV-vis absorption spectroscopy shows the intensity of the peak at certain wavelength which correlates to high molecular stacking; X-ray diffraction shows crystal reflection peaks implying where the molecular chains are oriented.

2. Effective liquid exfoliation of MoS_2

Liquid exfoliation methods have been diversely developed to enable the uniform dispersion of nanoparticles. The typical method includes at least two steps: sonication and centrifugation. The sonication applies ultrasonic sound into a solution, and help mixing nanoparticles into a solvent. The centrifugation separates a solution according to their size, density, and viscosity by centrifugal force. This method can effectively remove unexfoliated nanoparticles, and well-dispersed suspensions can be taken from the top layers. Moreover, reduced flake sizes can be achieved using ultrasonic milling if applicable. Implementing an additional exfoliation step to our hybrid ink formulation would give high quality MoS_2 dispersion in P3HT solution without large particles or aggregations.

3. Improving the electrode-semiconductor interface

The threshold voltages are known to be altered by traps existing at the interfaces of dielectric-semiconductor or electrode-semiconductor. In this research, the dielectric-semiconductor

interfaces of fabricated TFTs are modified with SAM, and the result implies that the film quality at the interface is improved. Hence, an improvement in the electrode-semiconductor interface is expected to enhance the electrical performance of the device further. Especially, due to the work function or energy level difference of an electrode material and a semiconductor material, the electrode-semiconductor interface act as an injection barrier for carriers. This barrier can be lowered by coating a polymer layer at the interface to adjust energy difference between two materials or SAM treatment on electrodes to modify work function.

References

[1] A. Daami *et al.*, "Fully printed organic CMOS technology on plastic substrates for digital and analog applications," in *2011 IEEE International Solid-State Circuits Conference*, 2011, pp. 328–330.

[2] S. Chung, S. O. Kim, S. K. Kwon, C. Lee, and Y. Hong, "All-inkjet-printed organic thin-film transistor inverter on flexible plastic substrate," *IEEE Electron Device Lett.*, vol. 32, no. 8, pp. 1134–1136, 2011.

[3] J. Kwon, Y. Takeda, K. Fukuda, K. Cho, S. Tokito, and S. Jung, "Three-Dimensional, Inkjet-Printed Organic Transistors and Integrated Circuits with 100% Yield, High Uniformity, and Long-Term Stability," *ACS Nano*, vol. 10, no. 11, pp. 10324–10330, 2016.

[4] T. Shimoda, K. Morii, S. Seki, and H. Kiguchi, "Inkjet Printing of Light-Emitting Polymer Displays," *MRS Bull.*, vol. 28, no. 11, pp. 821–827, Nov. 2003.

[5] C. N. Hoth, P. Schilinsky, S. A. Choulis, and C. J. Brabec, "Printing Highly Efficient Organic Solar Cells," *Nano Lett.*, vol. 8, no. 9, pp. 2806–2813, Sep. 2008.

[6] S. Jung, A. Sou, E. Gili, and H. Sirringhaus, "Inkjet-printed resistors with a wide resistance range for printed read-only memory applications," *Org. Electron.*, vol. 14, no. 3, pp. 699–702, 2013.

[7] G. S. Ryu, J. S. Kim, S. H. Jeong, and C. K. Song, "A printed OTFT-backplane for AMOLED display," *Org. Electron.*, vol. 14, no. 4, pp. 1218–1224, 2013.

[8] A. S. G. Reddy, B. B. Narakathu, M. Z. Atashbar, M. Rebros, E. Rebrosova, and M. K. Joyce, "Fully Printed Flexible Humidity Sensor," *Procedia Eng.*, vol. 25, pp. 120–123, 2011.

[9] F. Torrisi *et al.*, "Inkjet-printed graphene electronics," *ACS Nano*, vol. 6, no. 4, pp. 2992–3006, 2012.

[10] J. H. Chen, M. Ishigami, C. Jang, D. R. Hines, M. S. Fuhrer, and E. D. Williams, "Printed graphene circuits," *Adv. Mater.*, vol. 19, no. 21, pp. 3623–3627, 2007.

[11] T. Carey *et al.*, "Fully inkjet-printed two-dimensional material field-effect heterojunctions for wearable and textile electronics," *Nat. Commun.*, vol. 8, no. 1, 2017.

[12] E. Gracia-Espino *et al.*, "Electrical transport and field-effect transistors using inkjet-printed SWCNT films having different functional side groups," *ACS Nano*, vol. 4, no. 6, pp. 3318–3324, 2010.

[13] S. Chung, K. Cho, and T. Lee, "Recent Progress in Inkjet-Printed Thin-Film Transistors," *Adv. Sci.*, vol. 6, no. 6, p. 1801445, Mar. 2019.

[14] C. W. Tang, "Two-layer organic photovoltaic cell," *Appl. Phys. Lett.*, vol. 48, no. 2, pp. 183–185, 1986.

[15] C. W. Tang and S. A. Vanslyke, "Organic electroluminescent diodes," *Appl. Phys. Lett.*, vol. 51, no. 12, pp. 913–915, 1987.

[16] A. Tsumura, H. Koezuka, and T. Ando, "Macromolecular electronic device: Field-effect transistor with a polythiophene thin film," *Appl. Phys. Lett.*, vol. 49, no. 18, pp. 1210–1212, 1986.

[17] G. Horowitz, R. Hajlaoui, H. Bouchriha, R. Bourguiga, and M. Hajlaoui, "Concept of `threshold voltage' in organic field-effect transistors," *Adv. Mater.*, vol. 10, no. 12, pp. 923–927, 1998.

[18] K. P. Pernstich *et al.*, "Threshold voltage shift in organic field effect transistors by dipole monolayers on

the gate insulator," *J. Appl. Phys.*, vol. 96, no. 11, pp. 6431–6438, 2004.

[19] C. R. Newman, C. D. Frisbie, D. A. da Silva Filho, J.-L. Brédas, P. C. Ewbank, and K. R. Mann, "Introduction to Organic Thin Film Transistors and Design of n-Channel Organic Semiconductors," *Chem. Mater.*, vol. 16, no. 23, pp. 4436–4451, Nov. 2004.

[20] D. Braga and G. Horowitz, "High-Performance organic field-effect transistors," *Adv. Mater.*, vol. 21, no. 14–15, pp. 1473–1486, 2009.

[21] W. Petasch, B. Kegel, H. Schmid, K. Lendenmann, and H. U. Keller, "Low-pressure plasma cleaning: A process for precision cleaning applications," *Surf. Coatings Technol.*, vol. 97, no. 1–3, pp. 176–181, 1997.

[22] J. C. Love, L. A. Estroff, J. K. Kriebel, R. G. Nuzzo, and G. M. Whitesides, "Self-Assembled Monolayers of Thiolates on Metals as a Form of Nanotechnology," *Chem. Rev.*, vol. 105, no. 4, pp. 1103–1170, Apr. 2005.

[23] D. O. Hutchins *et al.*, "Effects of self-assembled monolayer structural order, surface homogeneity and surface energy on pentacene morphology and thin film transistor device performance," *J. Mater. Chem. C*, vol. 1, no. 1, pp. 101–113, 2013.

[24] Y. Wu *et al.*, "Controlled orientation of liquid-crystalline polythiophene semiconductors for high-performance organic thin-film transistors," *Appl. Phys. Lett.*, vol. 86, no. 14, pp. 1–3, 2005.

[25] A. Salleo, M. L. Chabinyc, M. S. Yang, and R. A. Street, "Polymer thin-film transistors with chemically modified dielectric interfaces," *Appl. Phys. Lett.*, vol. 81, no. 23, pp. 4383–4385, 2002.

[26] B. S. Ong, Y. Wu, P. Liu, and S. Gardner, "High-Performance Semiconducting Polythiophenes for Organic Thin-Film Transistors," *J. Am. Chem. Soc.*, vol. 126, no. 11, pp. 3378–3379, 2004.

[27] N. Tasaltin, D. Sanli, A. Jonáš, A. Kiraz, and C. Erkey, "Preparation and characterization of superhydrophobic surfaces based on hexamethyldisilazane-modified nanoporous alumina," *Nanoscale Res. Lett.*, vol. 6, pp. 1–8, 2011.

[28] D. E. King, "Oxidation of gold by ultraviolet light and ozone at 25 °C," *J. Vac. Sci. Technol. A Vacuum, Surfaces, Film.*, vol. 13, no. 3, pp. 1247–1253, 1995.

[29] J. Youn, G. R. Dholakia, H. Huang, J. W. Hennek, A. Facchetti, and T. J. Marks, "Influence of thiol self-assembled monolayer processing on bottom-contact thin-film transistors based on n-type organic semiconductors," *Adv. Funct. Mater.*, vol. 22, no. 9, pp. 1856–1869, 2012.

[30] J. F. Chang *et al.*, "Enhanced Mobility of poly(3-hexylthiophene) transistors by spin-coating from high-boiling-point solvents," *Chem. Mater.*, vol. 16, no. 23, pp. 4772–4776, 2004.

[31] B. Gburek and V. Wagner, "Influence of the semiconductor thickness on the charge carrier mobility in P3HT organic field-effect transistors in top-gate architecture on flexible substrates," *Org. Electron. physics, Mater. Appl.*, vol. 11, no. 5, pp. 814–819, 2010.

[32] H. Jia, S. Gowrisanker, G. K. Pant, R. M. Wallace, and B. E. Gnade, "Effect of poly (3-hexylthiophene) film thickness on organic thin film transistor properties," *J. Vac. Sci. Technol. A Vacuum, Surfaces, Film.*, vol. 24, no. 4, pp. 1228–1232, 2006.

[33] W. Li, H. E. Katz, A. J. Lovinger, and J. G. Laquindanum, "Field-effect transistors based on thiophene hexamer analogues with diminished electron donor strength," *Chem. Mater.*, vol. 11, no. 2, pp. 458–465, 1999.

[34] Z. Bao, A. Dodabalapur, and A. J. Lovinger, "Soluble and processable regioregular poly(3-hexylthiophene) for thin film field-effect transistor applications with high mobility," *Appl. Phys. Lett.*, vol. 69, no. 26, pp. 4108–4110, 1996.

[35] A. L. Briseno, F. S. Kim, A. Babel, Y. Xia, and S. A. Jenekhe, "N-Channel polymer thin film transistors with long-term air-stability and durability and their use in complementary inverters," *J. Mater. Chem.*, vol. 21, no. 41, pp. 16461–16466, 2011.

[36] B. Kang, W. H. Lee, and K. Cho, "Recent advances in organic transistor printing processes," *ACS Appl. Mater. Interfaces*, vol. 5, no. 7, pp. 2302–2315, 2013.

[37] J. Perelaer *et al.*, "Printed electronics: The challenges involved in printing devices, interconnects, and contacts based on inorganic materials," *J. Mater. Chem.*, vol. 20, no. 39, pp. 8446–8453, 2010.

[38] H. E. Katz, "Recent advances in semiconductor performance and printing processes for organic transistor-based electronics," *Chem. Mater.*, vol. 16, no. 23, pp. 4748–4756, 2004.

[39] S. Khan, L. Lorenzelli, and R. S. Dahiya, "Technologies for printing sensors and electronics over large flexible substrates: A review," *IEEE Sens. J.*, vol. 15, no. 6, pp. 3164–3185, 2015.

[40] K. Nomura, H. Ohta, A. Takagi, T. Kamiya, M. Hirano, and H. Hosono, "Room-temperature fabrication of transparent flexible thin-film transistors using amorphous oxide semiconductors," *Nature*, vol. 432, no. 7016, pp. 488–492, Nov. 2004.

[41] E. B. Secor, S. Lim, H. Zhang, C. D. Frisbie, L. F. Francis, and M. C. Hersam, "Gravure printing of graphene for large-area flexible electronics," *Adv. Mater.*, vol. 26, no. 26, pp. 4533–4538, 2014.

[42] P. Kopola, M. Tuomikoski, R. Suhonen, and A. Maaninen, "Gravure printed organic light emitting diodes for lighting applications," *Thin Solid Films*, vol. 517, no. 19, pp. 5757–5762, 2009.

[43] S. E. Burns, P. Cain, J. Mills, J. Wang, and H. Sirringhaus, "Inkjet Printing of Polymer Thin-Film Transistor Circuits," *MRS Bull*, vol. 28, no. 11, pp. 829–834, 2003.

[44] J. A. Lim *et al.*, "Inkjet-printed single-droplet organic transistors based on semiconductor nanowires embedded in insulating polymers," *Adv. Funct. Mater.*, vol. 20, no. 19, pp. 3292–3297, 2010.

[45] J. A. Lewis and B. Y. Ahn, "Three-dimensional printed electronics," *Nature*, vol. 518, no. 7537, pp. 42–43, Feb. 2015.

[46] A. Sridhar, T. Blaudeck, and R. R. Baumann, "Inkjet printing as a key enabling technology for printed electronics.," *Mater. Matters (Milwaukee, WI, United States)*, vol. 6, no. 1, pp. 12–17, 2011.

[47] C. H. Wu and W. S. Hwang, "The effect of the echo-time of a bipolar pulse waveform on molten metallic droplet formation by squeeze mode piezoelectric inkjet printing," *Microelectron. Reliab.*, vol. 55, no. 3–4, pp. 630–636, 2015.

[48] B. Derby, "Inkjet Printing of Functional and Structural Materials: Fluid Property Requirements, Feature Stability, and Resolution," *Annu. Rev. Mater. Res.*, vol. 40, no. 1, pp. 395–414, Jun. 2010.

[49] P. C. Duineveld, "The stability of ink-jet printed lines of liquid with zero receding contact angle on a homogeneous substrate," *J. Fluid Mech.*, vol. 477, no. 477, pp. 175–200, 2003.

[50] A. Assadi, C. Svensson, M. Willander, and O. Inganäs, "Field-effect mobility of poly(3-hexylthiophene)," *Appl. Phys. Lett.*, vol. 53, no. 3, pp. 195–197, Jul. 1988.

[51] H. Yan *et al.*, "A high-mobility electron-transporting polymer for printed transistors," *Nature*, vol. 457, no. 7230, pp. 679–686, 2009.

[52] J. W. Ward, Z. A. Lamport, and O. D. Jurchescu, "Versatile Organic Transistors by Solution Processing," *ChemPhysChem*, vol. 16, no. 6, pp. 1118–1132, Apr. 2015.

[53] P. Schilinsky, C. Waldauf, and C. J. Brabec, "Recombination and loss analysis in polythiophene based bulk heterojunction photodetectors," *Appl. Phys. Lett.*, vol. 81, no. 20, pp. 3885–3887, 2002.

[54] A. A. Virkar, S. Mannsfeld, Z. Bao, and N. Stingelin, "Organic semiconductor growth and morphology considerations for organic thin-film transistors," *Adv. Mater.*, vol. 22, no. 34, pp. 3857–3875, 2010.

[55] H. Sirringhaus *et al.*, "Two-dimensional charge transport in self-organized, high-mobility conjugated polymers," *Nature*, vol. 401, no. 6754, pp. 685–688, Oct. 1999.

[56] K. Tremel and S. Ludwigs, *P3HT Revisited – From Molecular Scale to Solar Cell Devices*, vol. 265. Berlin, Heidelberg: Springer Berlin Heidelberg, 2014.

[57] G. A. Salvatore *et al.*, "Fabrication and transfer of flexible few-layers MoS2 thin film transistors to any arbitrary substrate," *ACS Nano*, vol. 7, no. 10, pp. 8809–8815, 2013.

[58] R. Ganatra and Q. Zhang, "Few-Layer MoS 2 : A Promising Layered Semiconductor," *ACS Nano*, vol. 8, no. 5, pp. 4074–4099, May 2014.

[59] K. K. Kam and B. A. Parkinson, "Detailed photocurrent spectroscopy of the semiconducting group VI transition metal dichalcogenides," *J. Phys. Chem.*, vol. 86, no. 4, pp. 463–467, 1982.

[60] K. F. Mak, C. Lee, J. Hone, J. Shan, and T. F. Heinz, "Atomically thin MoS2: A new direct-gap semiconductor," *Phys. Rev. Lett.*, vol. 105, no. 13, pp. 2–5, 2010.

[61] C. Ataca, H. Şahin, and S. Ciraci, "Stable, single-layer MX 2 transition-metal oxides and dichalcogenides in a honeycomb-like structure," *J. Phys. Chem. C*, vol. 116, no. 16, pp. 8983–8999, 2012.

[62] K. S. Novoselov *et al.*, "Two-dimensional atomic crystals," *Proc. Natl. Acad. Sci. U. S. A.*, vol. 102, no. 30, pp. 10451–10453, 2005.

[63] P. Joensen, R. F. Frindt, and S. R. Morrison, "Single-layer MoS2," *Mater. Res. Bull.*, vol. 21, no. 4, pp. 457–461, 1986.

[64] J. N. Coleman *et al.*, "Two-Dimensional Nanosheets Produced by Liquid Exfoliation of Layered Materials," *Science (80-.).*, vol. 331, no. 6017, pp. 568–571, Feb. 2011.

[65] R. J. Smith *et al.*, "Large-scale exfoliation of inorganic layered compounds in aqueous surfactant solutions," *Adv. Mater.*, vol. 23, no. 34, pp. 3944–3948, 2011.

[66] J. Huang *et al.*, "Polymeric semiconductor/graphene hybrid field-effect transistors," *Org. Electron. physics, Mater. Appl.*, vol. 12, no. 9, pp. 1471–1476, 2011.

[67] P. Yadav, C. Chanmal, A. Basu, L. Mandal, J. Jog, and S. Ogale, "Catalyst free novel synthesis of graphene and its application in high current OFET and phototransistor based on P3HT/G composite," *RSC Adv.*, vol. 3, no. 39, pp. 18049–18054, 2013.

[68] A. Liscio *et al.*, "Charge transport in graphene-polythiophene blends as studied by Kelvin Probe Force Microscopy and transistor characterization," *J. Mater. Chem.*, vol. 21, no. 9, pp. 2924–2931, 2011.

[69] D. H. Kim *et al.*, "Design of a polymer-carbon nanohybrid junction by interface modeling for efficient printed transistors," *ACS Nano*, vol. 6, no. 1, pp. 662–670, 2012.

[70] C. H. Chang and C. H. Chien, "Functionalized single-walled carbon-nanotube-blended P3HT-based thin-film transistors with multiwalled carbon-nanotube source and drain electrodes," *IEEE Electron Device Lett.*, vol. 32, no. 10, pp. 1457–1459, 2011.

[71] X. Z. Bo, C. Y. Lee, M. S. Strano, M. Goldfinger, C. Nuckolls, and G. B. Blanchet, "Carbon nanotubes-semiconductor networks for organic electronics: The pickup stick transistor," *Appl. Phys. Lett.*, vol. 86, no. 18, pp. 1–3, 2005.

[72] S. Liu, S. C. B. Mannsfeld, M. C. LeMieux, H. W. Lee, and Z. Bao, "Organic semiconductor-carbon nanotube bundle bilayer field effect transistors with enhanced mobilities and high on/off ratios," *Appl. Phys. Lett.*, vol. 92, no. 5, p. 053306, Feb. 2008.

[73] J. López-Cuevas, E. Interial-Orejón, C. A. Gutiérrez-Chavarría, and J. C. Rendón-Ángeles, "Improved Performance p-type Polymer (P3HT) / n-type Nanotubes (WS2) Electrolyte Gated Thin- Film Transistor," *MRS Adv.*, vol. 2, no. 62, pp. 3865–3872, 2017.

[74] Z. Sun, J. Li, C. Liu, S. Yang, and F. Yan, "Enhancement of hole mobility of poly(3-hexylthiophene) induced by titania nanorods in composite films," *Adv. Mater.*, vol. 23, no. 32, pp. 3648–3652, 2011.

[75] T. Xie, G. Z. Xie, H. F. Du, Z. B. Ye, Y. J. Su, and Y. Y. Chen, "The mobility improvement of organic thin film transistors by introducing ZnO-nanrods as an zctive layer," *Sci. China Technol. Sci.*, vol. 59, no. 5, pp. 714–720, 2016.

[76] Y. Zhang *et al.*, "Two-dimensional MoS2-assisted immediate aggregation of poly-3-hexylthiophene with high mobility," *Phys. Chem. Chem. Phys.*, vol. 17, no. 41, pp. 27565–27572, 2015.

[77] Y. Kanai and J. C. Grossman, "Role of semiconducting and metallic tubes in P3HT/carbon-nanotube photovoltaic heterojunctions: Density functional theory calculations," *Nano Lett.*, vol. 8, no. 3, pp. 908–912, 2008.

[78] H. Hu and R. G. Larson, "Marangoni Effect Reverses Coffee-Ring Depositions," *J. Phys. Chem. B*, vol. 110, no. 14, pp. 7090–7094, Apr. 2006.

[79] M. Majumder *et al.*, "Overcoming the 'coffee-stain' effect by compositional marangoni-flow-assisted drop-drying," *J. Phys. Chem. B*, vol. 116, no. 22, pp. 6536–6542, 2012.

[80] J. M. Walls and R. Smith, *Surface Science Techniques*, vol. 51, no. 6–7. Berlin, Heidelberg: Springer Berlin Heidelberg, 2013.

[81] J. A. Powell *et al.*, "Temperature dependent solubility of gold nanoparticle suspension/solutions," *RSC Adv.*, vol. 6, no. 74, pp. 70638–70643, 2016.

[82] Y. H. Kim *et al.*, "Ultrasensitive reversible oxygen sensing by using liquid-exfoliated MoS2 nanoparticles," *J. Mater. Chem. A*, vol. 4, no. 16, pp. 6070–6076, 2016.

[83] D. H. Kim, H. S. Lee, H. Yang, L. Yang, and K. Cho, "Tunable crystal nanostructures of pentacene thin films on gate dielectrics possessing surface-order control," *Adv. Funct. Mater.*, vol. 18, no. 9, pp. 1363–1370, 2008.

[84] Y. Horii *et al.*, "Investigation of self-assembled monolayer treatment on SiO2 gate insulator of poly(3-hexylthiophene) thin-film transistors," *Thin Solid Films*, vol. 518, no. 2, pp. 642–646, 2009.

[85] Q. Zhou, Z. Jin, H. Li, and J. Wang, "Enhancing performance and uniformity of CH3NH3 PbI3-xClx perovskite solar cells by air-heated-oven assisted annealing under various humidities," *Sci. Rep.*, vol. 6, no. January, pp. 1–8, 2016.

[86] Y. Lin *et al.*, "Improved performances of inkjet-printed poly(3-hexylthiophene) organic thin-film transistors by inserting an ionic self-assembled monolayer," *RSC Adv.*, vol. 6, no. 47, pp. 40970–40974, 2016.

[87] B. Radisavljevic, A. Radenovic, J. Brivio, V. Giacometti, and A. Kis, "Single-layer MoS2 transistors," *Nat. Nanotechnol.*, vol. 6, no. 3, pp. 147–150, 2011.

[88] L. Mo *et al.*, "Silver nanoparticles based ink with moderate sintering in flexible and printed electronics," *Int. J. Mol. Sci.*, vol. 20, no. 9, 2019.

[89] R. D. Deegan, O. Bakajin, T. F. Dupont, G. Huber, S. R. Nagel, and T. A. Witten, "Capillary flow as the cause of ring stains from dried liquid drops," *Nature*, vol. 389, no. 6653, pp. 827–829, Oct. 1997.

[90] M. Egginger, S. Bauer, R. Schwödiauer, H. Neugebauer, and N. S. Sariciftci, "Current versus gate voltage hysteresis in organic field effect transistors," *Monatshefte fur Chemie*, vol. 140, no. 7, pp. 735–750, 2009.

[91] S. Liu, S. C. B. Mannsfeld, M. C. Lemieux, H. W. Lee, and Z. Bao, "Organic semiconductor-carbon nanotube bundle bilayer field effect transistors with enhanced mobilities and high on/off ratios," *Appl. Phys. Lett.*, vol. 92, no. 5, 2008.

[92] F. Xue, Z. Liu, Y. Su, and K. Varahramyan, "Inkjet printed silver source/drain electrodes for low-cost polymer thin film transistors," *Microelectron. Eng.*, vol. 83, no. 2, pp. 298–302, 2006.

[93] Y. Xu, H. Cao, Y. Xue, B. Li, and W. Cai, "Liquid-Phase Exfoliation of Graphene: An Overview on Exfoliation Media, Techniques, and Challenges," *Nanomaterials*, vol. 8, no. 11, p. 942, Nov. 2018.

[94] Q. H. Wang, K. Kalantar-Zadeh, A. Kis, J. N. Coleman, and M. S. Strano, "Electronics and optoelectronics of two-dimensional transition metal dichalcogenides," *Nat. Nanotechnol.*, vol. 7, no. 11, pp. 699–712, 2012.

[95] R. Ahmad, R. Srivastava, S. Yadav, S. Chand, and S. Sapra, "Functionalized 2D-MoS2-incorporated polymer ternary solar cells: Role of nanosheet-induced long-range ordering of polymer chains on charge transport," *ACS Appl. Mater. Interfaces*, vol. 9, no. 39, pp. 34111–34121, 2017.

[96] J. Xiao, M. Long, M. Li, X. Li, H. Xu, and K. Chan, "Carrier mobility of MoS2 nanoribbons with edge chemical modification," *Phys. Chem. Chem. Phys.*, vol. 17, no. 10, pp. 6865–6873, 2015.